



1 **Where does the dust deposited over the Sierra Nevada snow come from?**

2

3 Huilin Huang^{1*}, Yun Qian^{1*}, Ye Liu¹, Cenlin He², Jianyu Zheng^{3,4}, Zhibo Zhang^{3,4}, Antonis Gkikas⁵

4

5 ¹Atmospheric Sciences and Global Change Division, Pacific Northwest National Laboratory, Richland, WA,

6 USA

7 ²Research Applications Laboratory, National Center for Atmospheric Research, Boulder, CO, USA

8 ³Department of Physics, University of Maryland Baltimore County, Baltimore, MD, USA

9 ⁴Joint Center for Earth Systems Technology, University of Maryland Baltimore County, Baltimore, MD, USA

10 ⁵Institute for Astronomy, Astrophysics, Space Applications and Remote Sensing, National Observatory of

11 Athens, Athens, Greece

12

13 *Corresponding to: Huilin Huang, Huilin.huang@pnnl.gov; Yun Qian, Yun.Qian@pnnl.gov

14

15

16

17

18



19 **Abstract**

20 Mineral dust contributes up to one-half of surface aerosol loading in spring over the southwestern U.S.,
21 posing an environmental challenge that threatens human health and the ecosystem. Using the self-
22 organizing map (SOM) analysis, we identify four typical dust transport patterns across the Sierra Nevada,
23 associated with the mesoscale winds, Sierra-Block-Jets (SBJ), North-Pacific-High (NPH), and long-range
24 cross-Pacific westerlies, respectively. We find dust emitted from the Central Valley is persistently
25 transported eastward, while dust from the Mojave Desert and Great Basin influences the Sierra Nevada
26 during mesoscale transport occurring mostly in the winter and early spring. Asian dust reaching the
27 mountain range comes either from the west through straight isobars (cross-Pacific transport) or from the
28 north in the presence of NPH. Extensive dust depositions are found on the west slope of the mountain,
29 contributed by Central Valley emissions and cross-Pacific remote transport. Especially, the SBJ-related
30 transport produces deposition through landfalling atmospheric rivers, whose frequency might increase in a
31 warming climate.

32



33 **1. Introduction**

34 The emission, transport, and deposition of mineral dust (hereafter dust) are processes receiving
35 increasing interest from the scientific community (Sarangi et al., 2020). Dust emission is an integral part of
36 aridification and mirrors the effects of climatic change and anthropogenic land use on the dust-prone area
37 (Duniway et al., 2019). Airborne dust interacts with Earth’s climate system by altering radiation budget and
38 cloud lifetime and amount (Forster et al., 2007; Haywood et al., 2005; Huang et al., 2019). Its adverse
39 impacts on human health, ranging from cardiovascular illnesses to premature mortality, are well-
40 documented by numerous epidemiological studies (Laden et al., 2006; Lim et al., 2012; Crooks et al., 2016).
41 The deposition of dust on snow surface influences snow albedo, further contributing to anthropogenic
42 climate change as early as the 1970s (Qian et al., 2009; Qian et al., 2014; Skiles et al., 2018).

43 Dust over the southwestern U.S., particularly in California and Nevada states, is an important
44 aerosol type contributing to more than half of surface aerosol concentrations in spring (Kim et al., 2021).
45 Covered by dry soil with large gaps and sparse vegetation, the surrounding Mojave Desert, Sonoran Desert,
46 and Great basin are susceptible to wind erosion (Okin et al., 2006; Duniway et al., 2019). The dry or
47 ephemeral lakes in the deserts produce very fine dust containing toxic inorganic constituents (Goldstein et
48 al., 2017). In addition, anthropogenic land-use practices – e.g., agriculture and human settlement, have
49 greatly disturbed crustal biomass and produced windblown dust along the west coast (Pappagianis and
50 Einstein, 1978; Clausnitzer and Singer, 2000; Neff et al., 2008). Furthermore, cross-Pacific dust transported
51 from Asia and Africa to the Sierra Nevada range is widely reported (Ault et al., 2011; Creamean et al., 2014;
52 Creamean et al., 2013). The surface dust concentration has been found to increase in the past two decades
53 during spring at sites across the Southwest (Tong et al., 2017; Hand et al., 2017; Brahney et al., 2013), and
54 the onset of dust season is shifting earlier in response to climate change (Hand et al., 2016). The elevated
55 dust emission and earlier dust season are supposed to lead to a spectrum of environmental and societal
56 impacts in the most populated U.S. state. Especially, the resultant dust deposition on mountain snow
57 decreases snow albedo and produces a radiation forcing of 0-14.6 W m⁻² during the melting season (Huang
58 et al., 2022a), shifting snowmelt timing to earlier dates and further increasing California’s vulnerability to



59 water resource fluctuations (Wu et al., 2018; Huang et al., 2022b). With its complex terrains, frequently
60 varying microclimate, and coexisting sources from both local and remote regions, the Sierra Nevada area
61 is an interesting region for studying dust transport and its response to climate change.

62 Characterization of dust emission, transport, and deposition across the Sierra Nevada has been
63 investigated using various data. Isotopic analyses (i.e., concentrations of Pb, Nd) are widely used to
64 distinguish and quantify the respective contribution of dust emission from local (dried Owen Lakes),
65 regional (Central Valley and the Mojave Desert), and global sources (Asia and Africa) on the dust
66 deposition on the mountain (Muhs et al., 2007; Jardine et al., 2021; Aciego et al., 2017; Aarons et al., 2019).
67 Their source attribution has been generally confirmed by the analyses of dust particle size and composition
68 (Creamean et al., 2014; Creamean et al., 2013; Reheis and Kihl, 1995). The isotopic and composition
69 analyses have been commonly used with back-trajectory modeling to further identify the dust transport
70 pathway from the source to the deposition location (Vicars and Sickman, 2011; Creamean et al., 2014;
71 Creamean et al., 2013). Yet, these analyses generally retrieve dust sources in a short time and at a specific
72 location. Alternatively, ground-based measurement networks were established in the 1990s and provide
73 long-term trends of dust concentrations and the interannual variability across multiple sites (Hand et al.,
74 2017; Achakulwisut et al., 2017; Hand et al., 2016). However, they do not contain information on dust
75 origins and atmospheric conditions responsible for dust transport. Satellite retrievals were less commonly
76 used to study dust characteristics across the Sierra Nevada (Lei and Wang, 2014), mainly due to the poor
77 data coverage caused by cloud contamination in the region.

78 Global and regional climate-chemistry models have been widely used to understand the drives of
79 the variability of dust and quantify the role of regional and remote transport, filling the gaps in the
80 observations (Chin et al., 2002; Chin et al., 2007; Kim et al., 2021; Wu et al., 2017). While dust emissions
81 and transport have been generally studied, there lacks a connection between dust emissions from the source
82 region and the timing, location, and amount of dust deposition to the Sierra Nevada snow. The isotopic and
83 composition analyses attribute dust sources at a few sites. But to our knowledge, no regional
84 characterization has been conducted on how dust is transported to the Sierra Nevada after emissions from



85 adjacent drylands and remote continents and when, where, and how much depositions occur for dust
86 transported through different pathways. The connection between dust emissions, transport pathways, and
87 deposition to snow would facilitate the prediction of future changes in dust regimes and the corresponding
88 climate impact, enabling more efficient management practices. With a focus on the dust that influences the
89 Sierra Nevada, this study investigates 1) Where does the dust come from? 2) How is dust transported to the
90 mountain from the sources? 3) How is the dust deposited on the Sierra Nevada during spring, when the
91 dust-in-snow largely influences snow albedo and snowmelt? In consideration of both dust emission season
92 and mountain snow duration, we confine our study period from February to June 2019. We integrate models
93 and observations to understand how the dust deposition is linked to a specific source both surrounding and
94 far from the Sierra Nevada.

95

96 **2.1 Model and Reanalysis datasets**

97 **2.1.1 WRF-Chem configuration**

98 Table 1. Model configuration.

Atmospheric processes	WRF-Chem Configuration
Meteorological IC/LBCs	ERA5
Microphysics	Morrison double-moment
Radiation	RRTMG for both shortwave/longwave
Land surface	CLM4 with SNICAR
Surface layer	Revised MM5 Monin-Obukhov
Planetary boundary layer	YSU scheme
Cumulus	Grell-Freitas
Chemical driver	MOZART
Aerosol driver	MOSAIC 4-bin
Anthropogenic emission	NEI2017
Biogenic emission	MEGAN
Biomass burning emission	FINNv2.2
Dust emission	GOCART
Chemical IC/BC conditions	CAM-Chem

99



100 We used the WRF-Chem version 3.9 to study dust emission and transport across the Sierra Nevada.
101 The model setups (Table 1), including the physical schemes and emission inventory, follow Huang et al.
102 (2022a), which showed that the model captures the distribution and variation in aerosols reasonably well in
103 the study domain (126.12-112.86°W, 32.3-43.0°N). The Model of Ozone and Related chemical Tracers
104 (MOZART) chemistry module (Emmons et al., 2020) and the Model for Simulating Aerosol Interactions
105 and Chemistry with four bins (MOSAIC 4-bin) aerosol model (Zaveri and Peters, 1999) were applied, and
106 dust emissions were calculated “online” using the GOCART dust scheme (Ginoux et al., 2001). The
107 meteorological initial and lateral boundary conditions were derived from the ECMWF Reanalysis v5
108 (ERA5) at 0.25° horizontal resolution and 6 h temporal intervals (Hersbach et al., 2020). Spectral nudging
109 was employed with a timescale of 6 h above the PBL to reduce the drift between ERA5 reanalysis data and
110 WRF’s internal tendencies (Von Storch et al., 2000). The chemical initial and boundary conditions were
111 provided by CAM-Chem (Buchholz et al., 2019).

112 We applied the model to two nested domains (Fig. 1). Domain 1 (126.12-112.86°W, 32.3-43.0°N)
113 was configured to cover all of California, Nevada, and part of the surrounding states with 110 × 120 grid
114 cells at 10 km × 10 km horizontal resolution; the nested domain 2 covered the Sierra Nevada and
115 surrounding regions with a 2 km × 2 km resolution. The cumulus scheme is turned off in domain 2 with
116 convection-permitting resolution. We used 35 vertical model layers from the surface to 10 hPa with denser
117 layers at lower altitudes to resolve the PBL. The simulation period ranged from September 20, 2018, to
118 August 31, 2019.

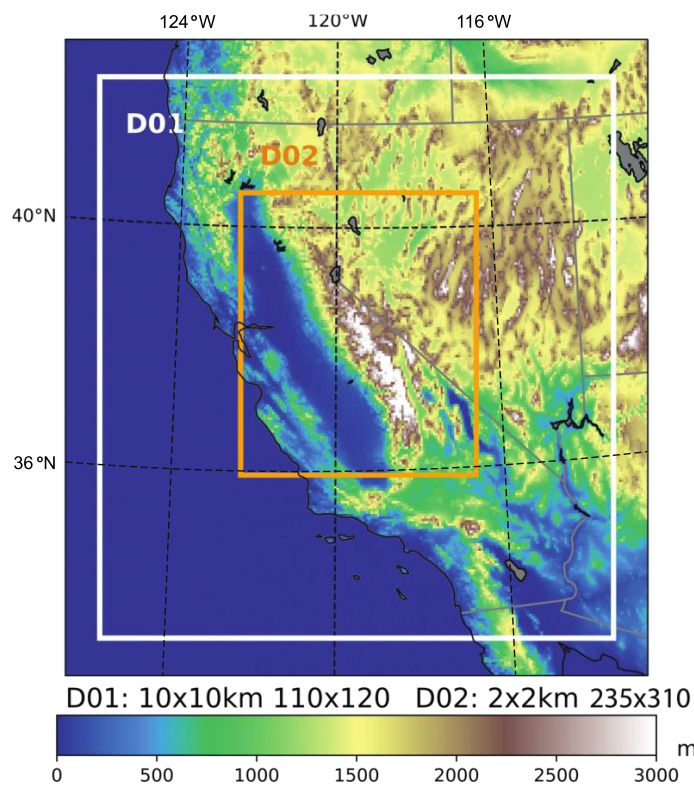


Figure 1 WRF-Chem simulation domain 1 (D01) and domain 2 (D02) used in this study

119
120
121

122 **2.1.2 MERRA-2 and ERA5 reanalysis**

123 The Modern-Era Retrospective analysis for Research and Applications, Version 2 (MERRA-2) is
124 a widely used atmospheric reanalysis with a spatial resolution of $0.500^{\circ} \times 0.625^{\circ}$ and 72 vertical layers
125 (Buchard et al., 2017). MERRA-2 aerosol products are produced by combining GEOS atmospheric model
126 version 5 (GEOS-5) with a 3D variational data assimilation algorithm to incorporate satellite observations,
127 including Advanced Very High Resolution Radiometer (AVHRR), Moderate Resolution Imaging
128 Spectroradiometer (MODIS), and Multi-angle Imaging Spectro Radiometer (MISR), as well as ground-
129 based observations such as the Aeronet RObotic NETwork (AERONET) (Gelaro et al., 2017). Although
130 the aerosol vertical profile, composition, and size distributions are not constrained by the assimilation of
131 aerosol optical depth (AOD), previous studies demonstrated that the aerosol assimilation system has
132 considerably improved the agreement with numerous observed aerosol properties (Buchard et al., 2016;



133 Buchard et al., 2017; Randles et al., 2017). The assimilation results in the imbalance of global dust mass
134 and produces a considerably larger deposition than the simulated dust emission (Buchard et al., 2017).
135 MERRA-2 simulates dust with diameter bins of 0.2–2.0 (DU001), 2.0–3.6 (DU002), 3.6–6.0 (DU003), 6.0–
136 12.0 (DU004), and 12.0–20.0 (DU005) μm , while the MOSAIC 4-bin in WRF-Chem simulates dust with
137 size bins of 0.039–0.156, 0.156–0.625, 0.625–2.5, and 2.5–10.0 μm . We therefore use the dust
138 concentrations of the first 4 size bins in MERRA-2 (DU001 + DU002 + DU003 + 0.74 * DU004) to match
139 with PM₁₀ dust concentration in WRF-Chem ([https://gmao.gsfc.nasa.gov/reanalysis/MERRA-](https://gmao.gsfc.nasa.gov/reanalysis/MERRA-2/FAQ/#Q5)
140 [2/FAQ/#Q5](https://gmao.gsfc.nasa.gov/reanalysis/MERRA-2/FAQ/#Q5)).

141 ERA5 provides assimilated wind fields at a $0.25^\circ \times 0.25^\circ$ horizontal resolution at 137 hybrid
142 sigma/pressure levels from 1979 to near real time (Hersbach et al., 2020). This study obtained the 3-hourly
143 meridional and zonal wind field from February to June 2019 from 1000 to 500 hPa. The ERA5 wind
144 reanalyses were used with satellite-retrieved dust optical depth (DOD) to evaluate the classified dust
145 emission and transport patterns from the model.

146

147 **2.2 Satellite observations for validation**

148 The Infrared Atmospheric Sounding Interferometer (IASI) onboarded European Meteorological
149 Operation (MetOp) satellite series measures infrared radiation in 8,461 spectral channels between 3.63 and
150 15.5 μm . The instrument provides near-global coverage with a spatial resolution of 12 km at nadir (Hilton
151 et al., 2012) since 2007. IASI is primarily sensitive to coarse mode dust particles, and thus the retrieved
152 AOD at the wavelength of 10 μm can represent the DOD (Yu et al., 2019). Note that the thermal infrared
153 (IR) AOD reported by IASI is usually significantly smaller than the visible AOD in MODIS, because of
154 the spectral dependence of dust extinction (Zheng et al., 2022). We use the version 2.2 AOD product
155 developed at the Centre National de la Recherche Scientifique Laboratoire de Météorologie Dynamique
156 from <https://iasi.aeris-data.fr/dust-aod/> (February 2022) (Capelle et al., 2014). The $0.3^\circ \times 0.3^\circ$ daily AOD
157 data covering California were produced by aggregating day and night retrievals at the satellite pixel



158 resolution (Capelle et al., 2018), in consideration of both data completeness and fine features. The $1.0^{\circ} \times 1.0^{\circ}$
159 daily AOD was produced in a similar way to investigate dust transport from Asia across the North Pacific.

160 The MIDAS (ModIs Dust AeroSol) dataset provides global fine-resolution ($0.1^{\circ} \times 0.1^{\circ}$) daily DOD
161 between 2003 and 2017 using quality-filtered AOD from MODIS Aqua and DOD-to-AOD ratios from
162 MERRA-2 reanalyses (Gkikas et al., 2021). Despite the uncertainties in modeled DOD-to-AOD ratios, the
163 validations of the MIDAS dataset against the AERONET dust-like AOD and the Lidar climatology of
164 Vertical Aerosol Structure for space-based lidar simulation (LIVAS) DOD reveal a high level of agreement
165 at both global and station level (Gkikas et al., 2022). Compared with other MODIS-derived DOD products
166 (Song et al., 2021; Voss and Evan, 2020; Ginoux et al., 2012; Pu and Ginoux, 2018), MIDAS has finer
167 spatial and temporal resolutions over both land and ocean, which is particularly applicable in this study
168 focusing on a small region and a few cases at daily scale. The dataset has been extended to near real-time
169 to match our study year.

170 Cloud-Aerosol Lidar with Orthogonal Polarization (CALIOP) is a two-wavelength (532 and 1064
171 nm) polarization lidar onboarded the Cloud-Aerosol Lidar and Infrared Pathfinder Satellite Observation
172 (CALIPSO) satellite (Hunt et al., 2009). Since June 2006, the lidar has been collecting an almost continuous
173 record of high-resolution profiles of aerosol and clouds as fine as 30 m in the vertical, covering 82°N to
174 82°S (Winker et al., 2010; Winker et al., 2009). This study used clear-sky data from the CALIOP Version
175 4, level-2 aerosol profile product (Young et al., 2018) to investigate the vertical profile of elevated dust
176 layer, especially from remote transport. When there were large DOD shown in IASI and MIDAS, we
177 examined the vertical profiles of dust by identifying the “dust,” “polluted dust,” and “dusty marine” species
178 in the CALIOP data (Kim et al., 2018)

179

180 **2.3 SOM analysis**

181 We applied the self-organizing map (SOM), a clustering method developed in the field of artificial
182 neural networks, to recognize different weather features associated with dust transport and deposition.
183 Similar to other clustering methods, SOM projects high-dimensional data into a two-dimensional grid. SOM



184 has been widely used in atmospheric sciences to recognize spatially organized sets of patterns in the data
185 (Reusch et al., 2007; Bao and Wallace, 2015; Liu et al., 2022; Song et al., 2019). Before the machine-
186 learning process, the initiation nodes are assigned randomly or more efficiently, as used here, selected from
187 the leading empirical orthogonal functions (EOFs). During the training phase, the Euclidean distance
188 between each input pattern and the initiation nodes is calculated to begin an iterative procedure. The best-
189 matching node or the “winning” node is the one with the smallest distance between the initiation nodes and
190 the input vector. Then the winning node and the neighborhood nodes around the winner are updated to
191 adjust themselves toward the input vector. Since this process is iterated and fine-tuned, the nodes are self-
192 organizing. The final SOM nodes represent typical dust transport and deposition patterns across the Sierra
193 Nevada.

194 Here, we first used five variables from WRF-Chem in the SOM clustering, including dust
195 deposition flux at the Sierra Nevada, the low-level meridional and zonal dust transport fluxes, and the mid-
196 level meridional and zonal dust transport fluxes surrounding the Sierra Nevada. The 3 hourly model outputs
197 during February-June 2019 are used to count for the spatial distribution and temporal evolution of dust
198 transport and deposition. For WRF-Chem, we averaged the zonal and meridional dust fluxes in levels 3-5
199 (roughly 875-925 hPa over coastal California) to acquire the low-level transport features and averaged 200-
200 700 hPa fluxes to acquire the mid-level features. Levels 3-5 were selected to focus on airborne particulate
201 matter entrained above the planetary boundary layer and transported on the regional scale. Remote transport
202 of Asian and African dust is mostly found around 600–200 hPa, which flows downward to the lower
203 troposphere along the post-cold isentropic surface into the atmospheric river (AR) environment (Voss et
204 al., 2021). By selecting levels between 200-700 hPa, we were able to include all cross-Pacific remote
205 transport in the middle level. The choice of how many SOM nodes to prescribe is a trade-off between
206 distinctiveness and robustness. We found four-nodes clustering captures distinct transport patterns, while
207 more nodes produce redundant clusters with similar patterns.

208 To verify the recognized transport patterns based on WRF-Chem, we conducted SOM analyses
209 using variables from MERRA-2. We first remapped the same five variables using bilinear interpolation



210 from $0.5^\circ \times 0.625^\circ$ to 10 km, the resolution of the WRF-Chem outer domain, before clustering. The vertical
211 levels of low-level and mid-level dust transport fluxes were selected to approximately match the WRF-
212 Chem pressure level. Four nodes were identified and arranged to make a direct comparison with those from
213 WRF-Chem. To further investigate if transport patterns recognized from SOM vary significantly with years,
214 we applied SOM analyses over 2011-2021 using MERRA-2 extended records of dust fluxes and deposition.

215

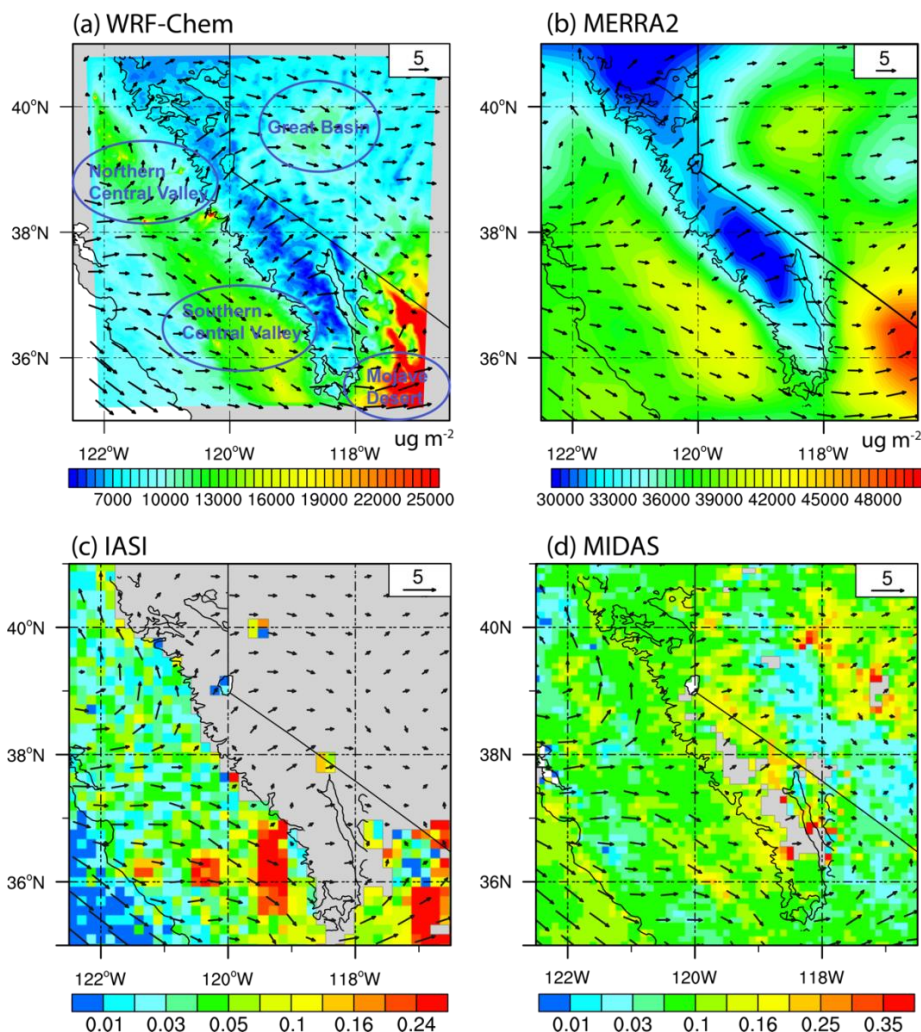
216 **3. Results**

217 **3.1 Dust emission sources around the Sierra Nevada**

218 We find four emission source regions surrounding the Sierra Nevada where dust emissions could
219 potentially influence the mountain snow impurities between February and June (Fig. 2). The Mojave Desert,
220 located southeast of the Sierra Nevada, is characterized by low annual precipitation, sparse vegetation, and
221 dried fine soil. Airborne dust loading over the desert can reach 30000 ug m^{-2} averaged over our study period
222 (Fig. 2a). It is generally transported eastward but can also be transported westward, influencing the southern
223 part of the mountain. Dust produced in the northern (Sacramento Valley) and the southern part (San Joaquin
224 and Tulare Basins) of the Central Valley is often transported eastward to the mountains. With high soil
225 aridity and a higher fraction of dry sand (Duniway et al., 2019), the southern Central Valley is more erodible
226 and emits a higher amount of fine dust. The Great Basin dust is relatively weak in magnitude but located at
227 a higher altitude. Therefore, it can easily ride along wind currents upward along the east slope of the
228 mountain. The column dust loading in MERRA-2 confirms our results in WRF-Chem (Fig. 2b), despite it
229 showing a stronger dust emission in the Great Basin while a weaker one in the Sacramento Valley. The
230 IASI shows the strongest IR DOD in the Mojave Desert, followed by the southern Central Valley, but
231 underestimates dust emissions from the Sacramento Valley (Fig. 2c). The underestimation is due to the fact
232 that IASI measures the radiation at IR wavelengths, which is more sensitive to coarse-mode dust particles
233 (Yu et al., 2019), whereas the fine dust produced in the Central Valley has a negligible contribution to DOD
234 at $10 \mu\text{m}$. In contrast, MIDAS captures dust emissions from the Great Basin, the southern and northern
235 Central Valley (Fig. 2d) but not the Mojave Desert. MIDAS is reported to underestimate DOD from the

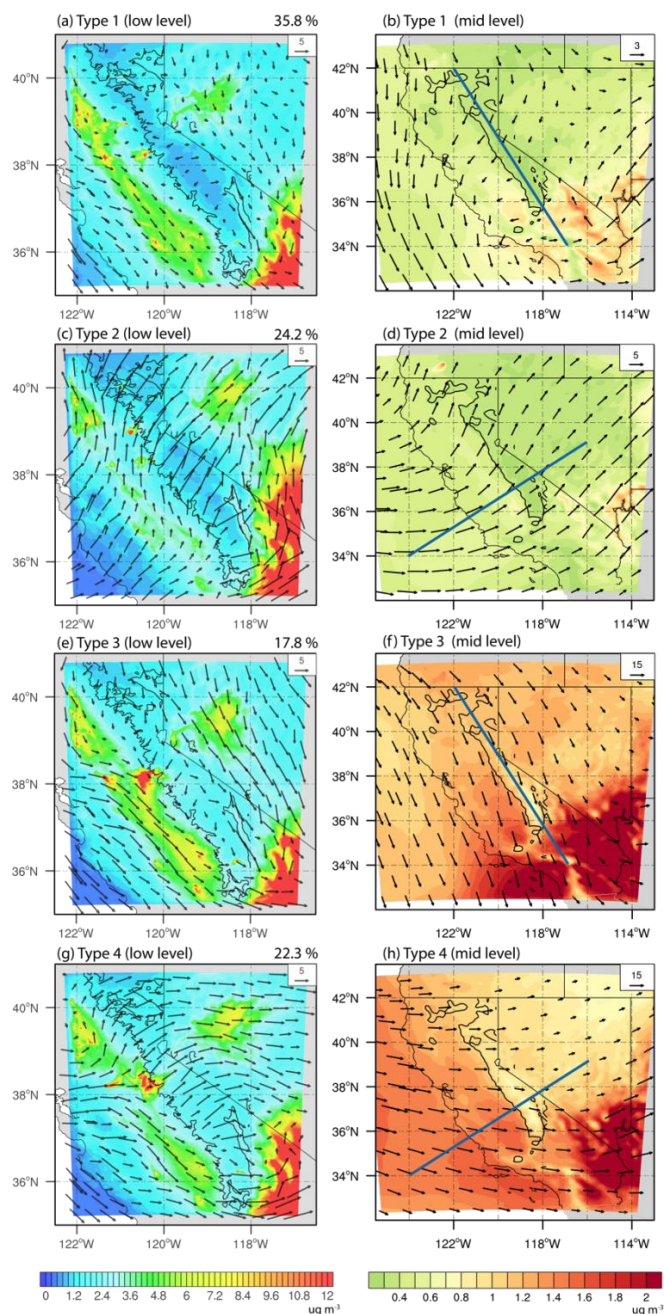


236 Mojave Desert (compared to AERONET DOD) as MERRA-2 simulates lower dust amounts there (Gkikas
 237 et al., 2021).



238 **Figure 2** The spatial distribution of dust in model and satellite observations averaged in 2019 February-
 239 June. Column dust loading (ug m^{-2}) and low-level winds (roughly 875-925 hPa; m s^{-1}) in (a) WRF-Chem
 240 and (b) MERRA-2. (c) Observed thermal infrared DOD at the wavelength of $10 \mu\text{m}$ from IASI (d) Observed
 241 visible DOD at the wavelength of $550 \mu\text{m}$ from MIDAS. The low-level winds (m s^{-1}) in (c) and (d) are from
 242 ERA5 reanalyses. Black contours indicate the elevation of 1500 m, which represents the Sierra Nevada
 243 range used in this study. The grey area in c-d are missing pixels in satellite observations
 244
 245

246 **3.2 Dust transport across the Sierra Nevada**



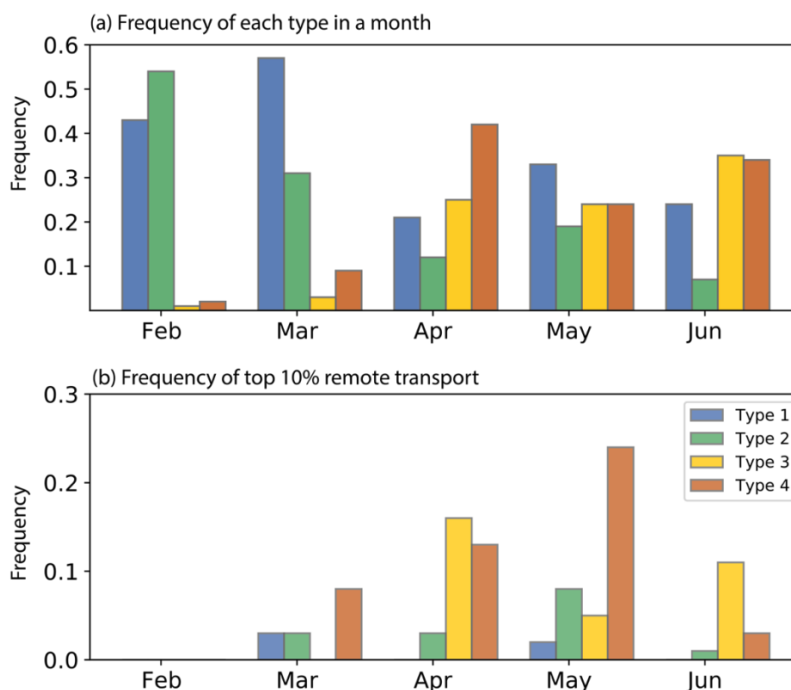
247
248
249
250
251
252

Figure 3 (a, c, e, g) Low-level (roughly 875-925 hPa) dust concentration ($\mu\text{g m}^{-3}$) and wind vectors (m s^{-1}) in each of the four SOM type in WRF-Chem; The numbers on the top right of subplots denote the frequency of each type. (b, d, f, h) Mid-level (200-700 hPa average) dust concentration ($\mu\text{g m}^{-3}$) and dust transport in types 1-4; The position of the cross-section used for Figure 5 is denoted in each plot.



253 This section introduces the features of dust transport patterns discerned from WRF-Chem and
 254 evaluates them against satellite observations over the period of February to June 2019. Figure 3 shows the
 255 WRF-Chem dust concentration and wind in the low levels and middle levels averaged for each of the four
 256 types acquired from the SOM analyses. The dust transport pattern represented in SOM type 1 accounts for
 257 35.8% of hours from February to June (Fig. 3a), especially in February (43%) and March (57%) (Fig. 4a).
 258 Type 2 occurs in 24.2% of the whole study period and contributes to more than 50% in February and then
 259 decreases with the month. In contrast, types 3 and 4 account for 17.8% and 22.3%, respectively, with the
 260 occurrence increasing with the month. The maximum occurrence is found in June for type 3 (40%) and
 261 April for type 4 (34%), respectively.

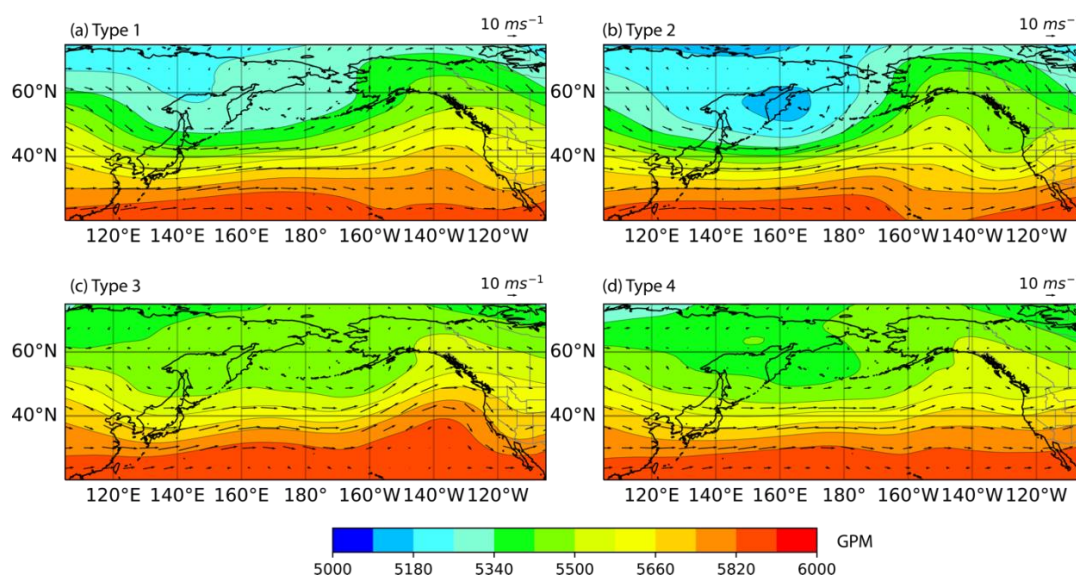
262 **3.2.1 Mesoscale regional (MSR) transport**



263 **Figure 4** (a) The frequency of each type (the time dominated by each type divided by total time in a month)
 264 that occurs in February, March, April, May, and June in WRF-Chem. (b) The frequency of each type in the
 265 top 10% remote transport (the time dominated by each type divided by total time of the top 10% remote
 266 transport).
 267
 268

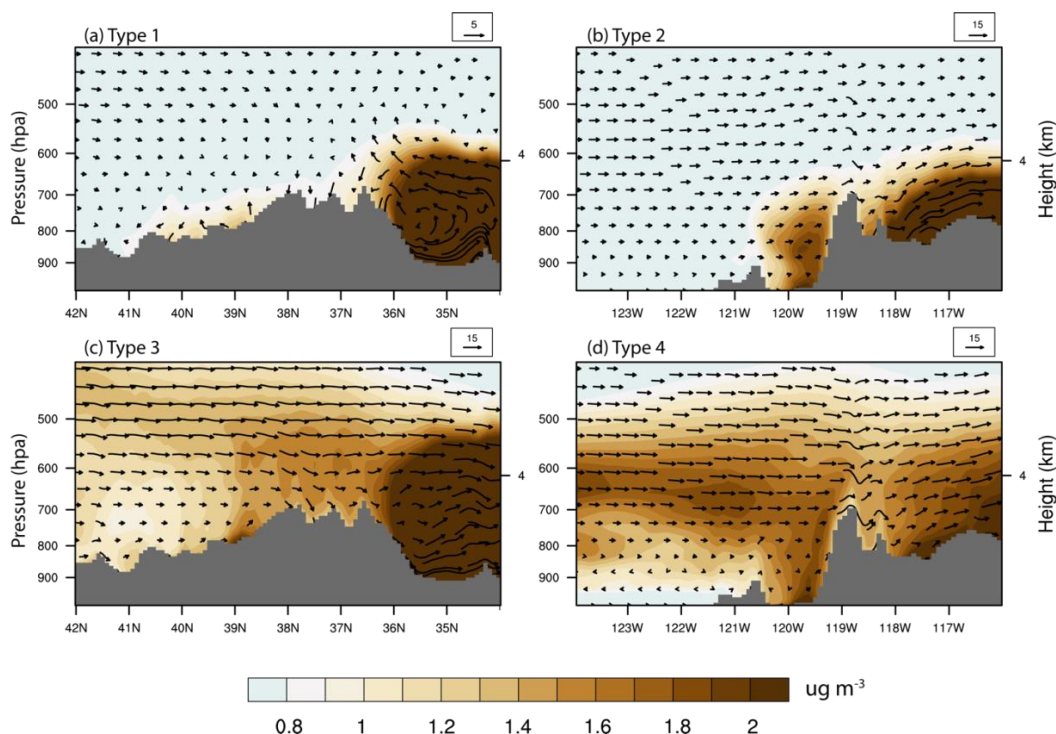


269 In type 1, dust is transported from northwest to southeast in the Central Valley in the low level
 270 (roughly 875-925 hPa over the California coast). A vortex (Schultz Eddy) was found in the northern Central
 271 Valley (Fig. 3a), circulating counter-clockwise and confining dust to the local environment (Bao et al.,
 272 2008). The air inflow from the ocean is relatively weak and obstructed by the terrain. The Great Basin is
 273 dominated by the northwesterlies. The emitted dust is transported southeastward and blocked by the
 274 mountain, depositing dust on the east slope. Dust emitted from the Mojave Desert can be elevated to the
 275 middle level (Fig. 3b). The cross-section further shows a vertical circulation where the Mojave Desert dust
 276 is blown away from the Sierra Nevada at the low level and towards the mountain at 600-700 hPa (Fig. 6a).
 277 A weaker mid-level cross-Pacific flow is found in type 1 than in other types (Fig. 5a), with no signals of
 278 remote transport reaching the Sierra Nevada (Fig. 3b). Type 1 generally corresponds to the dust transport
 279 in lack of prevailing large-scale weather systems. The high peaks of the Sierra Nevada produce mesoscale
 280 circulations and prevent the Central Valley and Great Basin dust from being transported to the other side
 281 of the mountain. It is referred to as the “mesoscale regional (MSR) transport” hereafter.



282
 283
 284

Figure 5 Geopotential height (gpm) and wind vectors (m s^{-1}) at 500 hPa in each of the four SOM types in WRF-Chem.



285
286
287
288
289
290

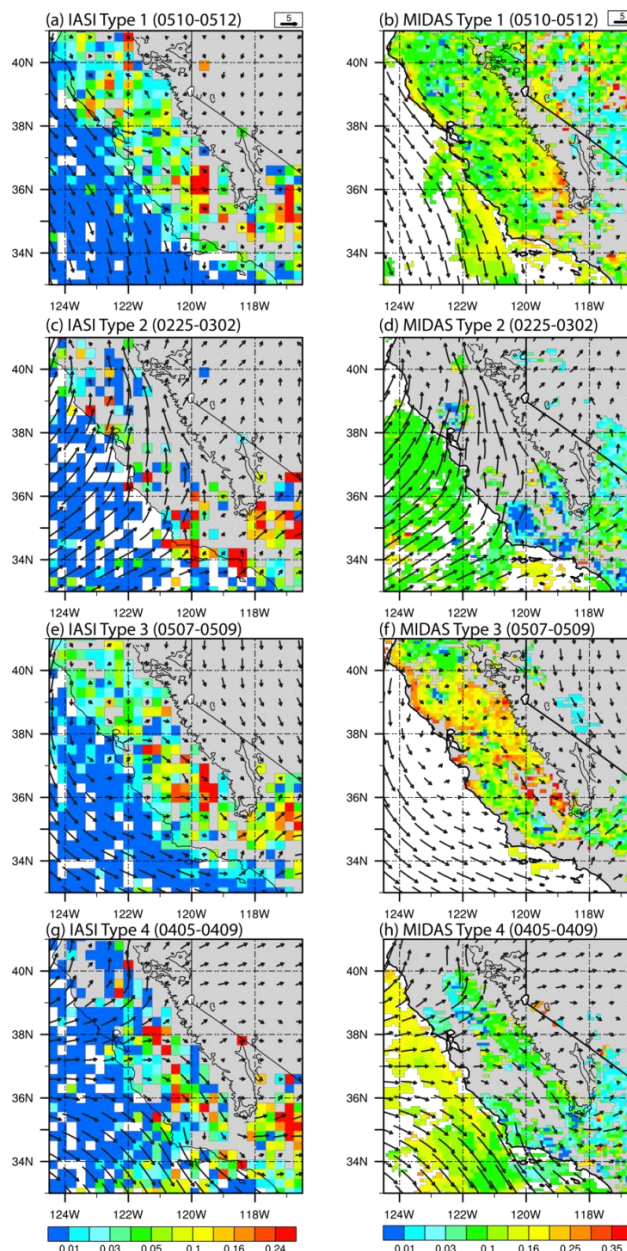
Figure 6 Cross-section of dust concentration (shaded; $\mu\text{g m}^{-3}$) and dust transport fluxes (vectors; $\mu\text{g m}^{-2} \text{s}^{-1}$) at 1000-400 hPa for each SOM type in WRF-Chem. The position of each cross-section is denoted in Fig. 3 b (Type 1), d (Type 2), f (Type 3), and h (Type 4). The grey area indicates the topography of the Sierra Nevada.

291
292
293
294
295
296
297
298
299
300

We validate the features of type 1 from WRF-Chem using satellite retrieved DOD and wind vectors from ERA5. The cloud contamination results in many missing satellite pixels in our study domain, making the transport patterns hard to discern on a single day. DOD and winds belonging to the same SOM type on consecutive days are averaged to maximize the data completeness. One typical example for each type is presented based on their representativeness and the maximum spatial coverage. Figures 7a-b present dust emission and transport patterns during May 10-12, a typical case for the MSR transport. In IASI, we find peak IR DOD (> 0.2) over the Mojave Desert and the southern Central Valley and moderate values in the Sacramento Basin related to the Schultz Eddy (Fig. 6a), resembling the relative magnitude of dust concentrations in regional source regions in WRF-Chem (Fig. 3a). MIDAS shows another evidence of dust transport pathways within the Central Valley with a higher resolution, although the maximum DOD shifts



301 slightly towards the mountain range (Fig. 7b). Dust emissions from the Great Basin are weaker than those
302 from the southern Central Valley.



303
304
305
306
307

Figure 7 (a,c,e,g) IR DOD at the wavelength of 10 μm retrieved from IASI and (b,d,f,h) visible DOD at the wavelength of 550 μm from MIDAS for each type. The low-level winds (vectors; m s^{-1}) are obtained from the ERA5 reanalyses. The numbers in the parenthesis indicate the event time period for the year 2019.



308 **3.2.2 Sierra-barrier-jets-related (SBJ-related) transport**

309 In type 2, the low-level winds turn to the north above the western slope of the Sierra Nevada (Fig.
310 3c), which resembles the terrain-locked Sierra barrier jets (SBJs) typically observed during the presence of
311 ARs (Neiman et al., 2013). The large-scale pattern consists of a low 500hPa geopotential height (GPH)
312 center in the north Pacific (Fig. 5b). The meridional gradient produces intense storm tracks from Kuroshio
313 Current towards Alaska. Indeed, we find extensive precipitations in type 2 (not shown), which produce
314 more wet deposition along the mountain's west slope and result in cleaner air in the Central Valley (Fig.
315 3c). The dust layer at the Central Valley is found below 700 hPa, mostly blocked by the high mountain
316 peaks and is hardly transported to the east slope of the mountain (Fig. 6b), despite the cross-barrier
317 westerlies found in the middle level. Dominated by SBJs, dust generated in the Great Basin and the Mojave
318 Desert is blown away from the mountain. No clear signal of remote transport is found on the California
319 coast (Fig. 3d). The dust transport from all sources is closely connected to SBJ; therefore, type 2 is referred
320 to as the "SBJ-related" transport. In both IASI and MIDAS, we find more missing pixels for SBJ-related
321 transport than any other type caused by cloud contamination (Figs. 7c-d). The AR-related landfalling
322 precipitations from February 25 to March 2 remove the airborne dust particles. A cleaner atmosphere might
323 be induced, but it is hard to confirm considering the missing pixels over the continent.

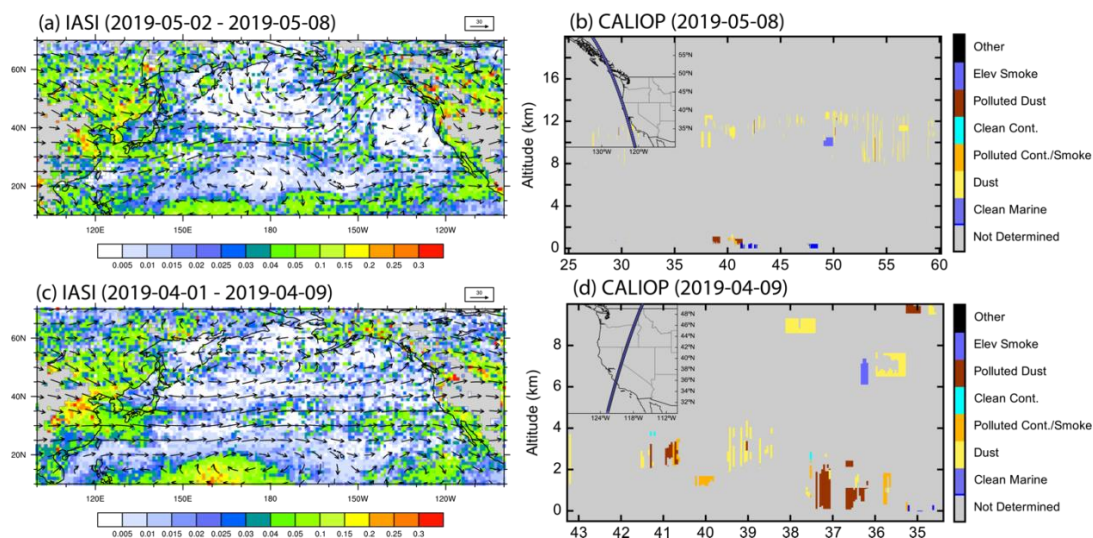
324 **3.2.3 North-Pacific-High-related (NPH-related) transport**

325 Type 3 has northwestern winds in both Central Valley and the Great Basin (Fig. 3e), transporting
326 Central Valley dust to the southwest part of the Sierra Nevada in early summer. It is known as the "North-
327 Pacific-High-related (NPH-related)" transport, during which the North Pacific High (NPH) built up in the
328 north Pacific 130° W produces the northwest-southeast wind direction along the California coast (Fig. 5c),
329 influencing the transport patterns for dust emitted from the surrounding sources. At the middle level, we
330 observe a meridional mid-level dust transport pathway (Fig. 3f), which appears at 400-500 hPa in the
331 northern Sierra Nevada and descends to 700 hPa at 36-37 °N, the top of the southern Sierra Nevada (Fig.
332 6c). As there are no major dust sources in the Pacific Northwest, the mid-level dust presumably origins



333 from Asia (discussed further in section 3.2.3). The dust emitted from the Great basin is transported by the
 334 southward winds to the east slope of the mountains, while emissions from the Mojave Desert are transported
 335 away from the mountain range.

336 The simulated dust concentration and transport in the NPH-related transport are confirmed by DOD
 337 observations during May 7-9, with the transport pathway parallel to the California coast (Figs. 7e-f). Studies
 338 have shown two main pathways of Asian dust transport to North America during the spring months: (1)
 339 meridional excursions north into Alaska and then south along the U.S. west coast, and (2) zonal transport
 340 over the North Pacific Ocean (Creamean et al., 2014). With north-south dust transport at the middle level,
 341 the NPH-related transport characterizes the first pathway. To examine this hypothesis, we averaged the IR
 342 DOD and 500 hPa wind field over the North Pacific during May 2-9. We included a few days before the
 343 event (Fig. 8a) as it takes 7-10 days for dust to be transported from Asia to North America (Ault et al., 2011;
 344 Creamean et al., 2013). The dust transport pathway shows that after being emitted from East Asia and the
 345 Gobi Desert, dust is transported zonally to 150 °W, excusing north into Alaska/Canada and then traveling
 346 south along the U.S. west coast. An elevated dust belt from 8 km to 12 km is discerned over the North
 347 American coast (27 °N to 60 °N) from the CALIOP data, denoting the north-south transport of a thin dust
 348 layer through the middle level (Fig. 8b).



349



350 **Figure 8** (a) IR DOD from IASI and 500 hPa winds (m s^{-1}) from ERA5 over the North Pacific for a typical
351 Type 3 case averaged between 2019-05-02 to 2019-05-08 (b) latitude-height cross-section of aerosol
352 species from CALIOP on 2019-05-08 (Type 3); (c) same as (a) but for a typical Type 4 case averaged
353 between 2019-04-01 to 2019-04-09; (d) same as (a) but for a typical Type 4 case on 2019-04-09
354

355 **3.2.4 Cross-Pacific zonal (CPZ) transport**

356 Air inflows from the ocean enter California and diverge to the northern and southern branches in
357 type 4, transporting dust eastward across the Sierra Nevada (Fig. 3g). At the middle level, the low-GPH
358 center recedes in April, and the isobars become straighter than in boreal winter, which facilitates the zonal
359 transport of dust emitted from middle Asia over the North Pacific Ocean (Fig. 5d). The cross-section further
360 shows an elevated dust layer is transported from the ocean at around 700-500 hPa (Fig. 6d). The
361 concentrations are much stronger, and the altitude also lower than the NPH-related transport (Fig. 6c). The
362 remotely transported dust descends to low altitudes when reaching the California coast and converges with
363 the dust from the Central Valley at around 800 hPa. A portion of dust is compacted to the west slope at
364 higher elevations, and the remaining across the mountains affects the east slope. Dust emitted from the
365 Great Basin and the Mojave Desert is transported away from the mountains. Type 4 is denoted with “cross-
366 Pacific zonal (CPZ) transport” to reflect the strong cross-Pacific dust transport.

367 April 5-9, a typical case for the CPZ transport, clearly shows the north and south branches of dust
368 transport over the Central Valley (Figs. 7g-h). Different from the NPH-related transport pathway, the large-
369 scale DOD and winds at 500 hPa (averaged over April 1-9) show that dust emitted from East Asia is being
370 transported eastward, with a belt of IR DOD > 0.1 evident around 25-40 °N (Fig. 8c). The vertical
371 distribution shows an elevated dust layer at 2-4 km above ground level, reaching the higher elevation of the
372 mountain (Fig. 8d).

373 We calculated the mid-level dust remote transport, defined as the dust influxes from the north and
374 west boundaries of the 200-700 hPa of WRF-Chem modeling domain 1, and investigated how the top 10%
375 largest remote transport distribute in each SOM (Fig. 4b). Among all the large remote transport, CPZ
376 transport accounts for 48% while NPH-related accounts for 32%, indicating that the zonal pathway plays a
377 more important role in the cross-Pacific transport. Most remote transports are found in April and May, the



378 former dominated by the meridional transport in the existence of the NPH while the latter led by the CPZ
379 transport. The remaining two types contribute to a fairly small portion consistent with the clean atmosphere
380 in the middle levels (Figs. 3b, d).

381 To summarize, we discern four types of dust transport patterns across the Sierra Nevada and analyze
382 the monthly variability in their occurrence. The MSR transport represents the local dust transport, which
383 contributes to more than 20% of the time each month during February-June (Fig. 4a) in the absence of
384 prevailing weather systems. The SBJ-related air inflows transport dust eastward and are closely related to
385 the AR, during which the GPH and storm tracks at 500 hPa feature a typical large-scale pattern during the
386 boreal winter (Rodionov et al., 2007). As time evolves, the GPH center recedes, and the isobars become
387 more straight zonally in April, bringing dust from Asia and Africa to the western U.S. coast (CPZ transport).
388 In early summer, the buildup of NPH in the east Pacific corresponds to north-south winds along the
389 California coast, transporting dust along the Sierra Nevada (NPH-related transport).

390

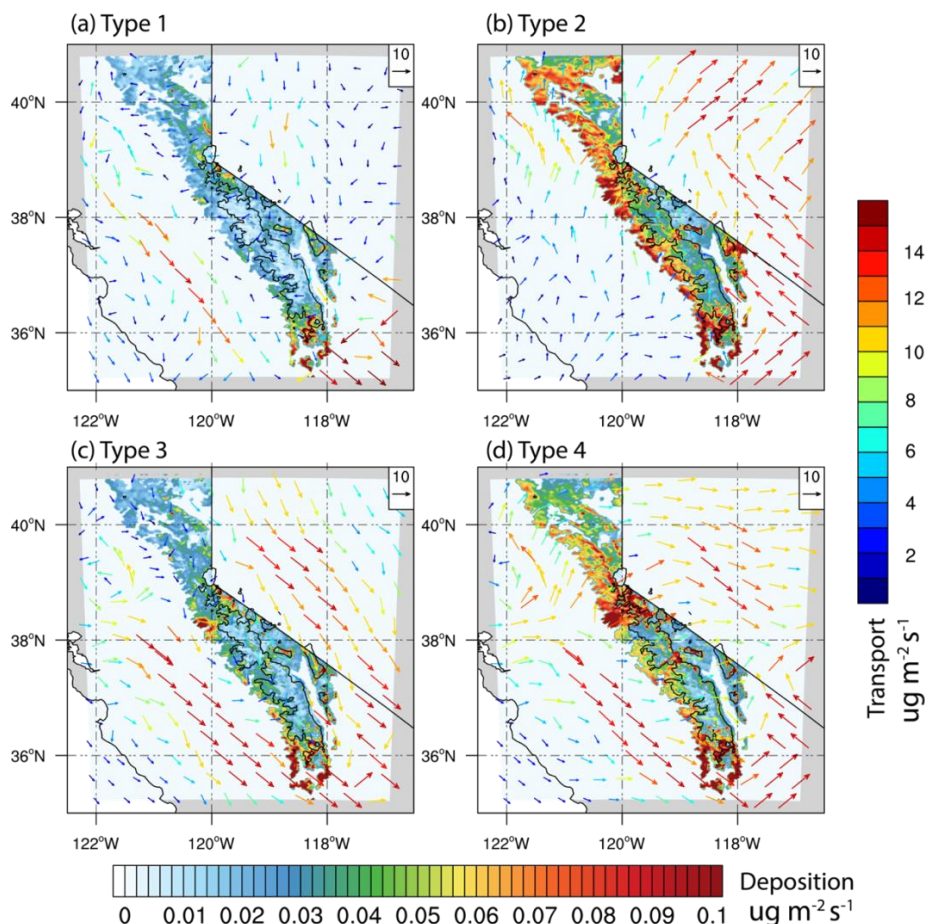
391 **3.3 Dust deposition over the Sierra Nevada**

392 The averaged dust deposition and low-level dust transport for each type are shown in Fig. 9, including
393 both dry and wet depositions. The dry depositions consider the diffusion and gravitational effects, while
394 wet depositions describe in-cloud removal (rainout) and below-cloud removal (washout) by grid-resolved
395 stratiform precipitation as well as the sub-grid wet scavenging (Chapman et al., 2009; Easter et al., 2004).
396 In all SOM types, extensive depositions are found on the west slope in all types, generally decreasing with
397 elevation.

398 The MSR transport has the smallest deposition among the four types (Fig. 9a). Large depositions are
399 found in the southern Sierra Nevada and Lake Tahoe. Dust contributing to the deposition origins mainly
400 from the Mojave Desert and the Great Basin dryland. In contrast, large depositions found in the southern
401 and eastern parts of the mountains in NPH-related transport may be produced in agricultural land from the



402 southern Central Valley, as we find a persistent eastward transport pathway in the low level (Fig. 9c). The
 403 remote transported dust plays a minor role as it is located above 8 km in altitude.



404
 405 **Figure 9** (a-d) Dust deposition (shaded; $\mu\text{g m}^{-2} \text{s}^{-1}$) over the Sierra Nevada and low-level dust transport
 406 fluxes (colored vectors; $\mu\text{g m}^{-2} \text{s}^{-1}$) across the Sierra Nevada averaged over each of the four SOM types in
 407 WRF-Chem. Black contours indicate an elevation of 2500 m. The bottom color bar shows the magnitude
 408 of dust deposition over the Sierra Nevada while the right color bar shows the magnitude of dust transport
 409 flux vectors.
 410

411 While SBJ-related transport has the lowest low-level dust concentration over the Central Valley, it
 412 produces the largest deposition along the west slope (Fig. 9b). Most eastward transport in the southern
 413 Sierra Nevada is obstructed by the high mountain peaks, resulting in large depositions below 2900 m. The
 414 SBJ turns eastward in the Sacramento Basins and climbs through the mountain north of 38 °N, producing



415 a relatively homogenous deposition in the northern part. The combination of dust transport and deposition
416 indicates that dust influencing the mountain snow impurities mostly comes from the Central Valley.
417 Compared with the other SOM types, SBJ-related transport has large depositions at elevations higher than
418 2500 m (discuss later). Large depositions are also found in the CPZ transport (Fig. 9d), with the largest
419 value occurring on the west slope of the central and southern Sierra Nevada, contributed by both Asian dust
420 and Central Valley dust. Compared to the MSR and NPH-related transport, the large-scale westerlies in the
421 Central Valley (SBJ-related and cross-Pacific transport) produce larger deposition, probably because of the
422 more efficient removal of particles by collision with terrestrial surfaces at higher elevations (Fig. 6d).

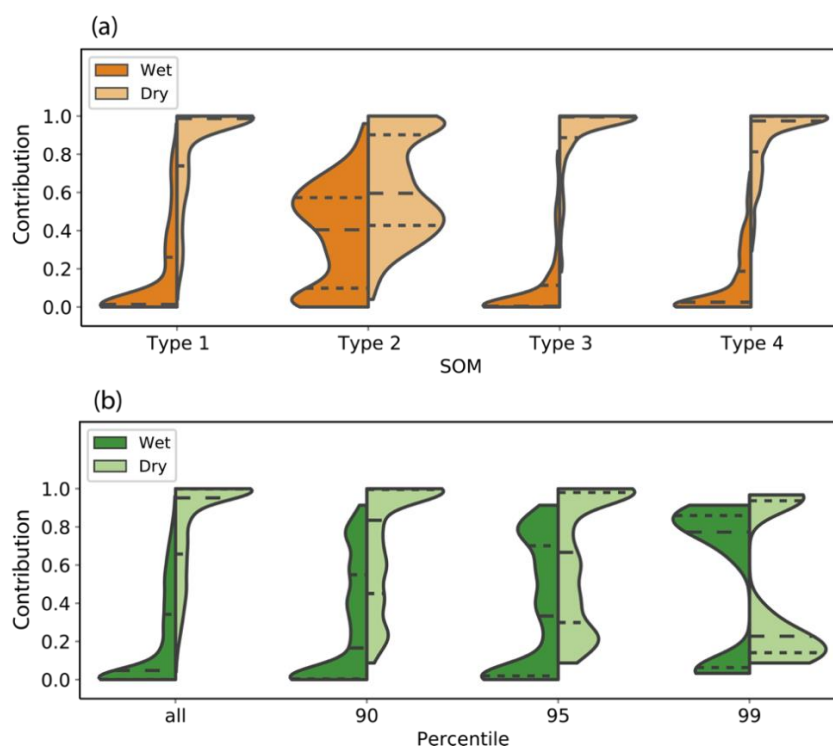
423 To quantify the relative importance of wet and dry depositions in each 3 hourly total deposition data,
424 we calculate the fraction of wet depositions to total depositions averaged over the Sierra Nevada:

425 $\frac{\text{Wet deposition}}{\text{Wet deposition} + \text{Dry deposition}}$. The contribution of dry deposition is defined in a similar way. We find the

426 wet deposition accounting for 40% in frequency in the SBJ-related type. The landfalling precipitation has
427 deposited large amounts of airborne dust on the snow surface, producing a cleaner atmosphere as we have
428 found in Fig. 3c. The frequent wet depositions also explain the larger depositions in high elevations (Fig.
429 9b): dust particles reaching the high mountains are small in size and difficult to deposit through gravitational
430 effects. Wet deposition is a more efficient way of depositing small particles as they collect dust in raindrops.

431 In contrast, the dry depositions play predominant roles (more than 80% in frequency) in all the other types
432 (Fig. 10a). Figure 10b further shows the contribution of wet deposition increases with deposition intensity.

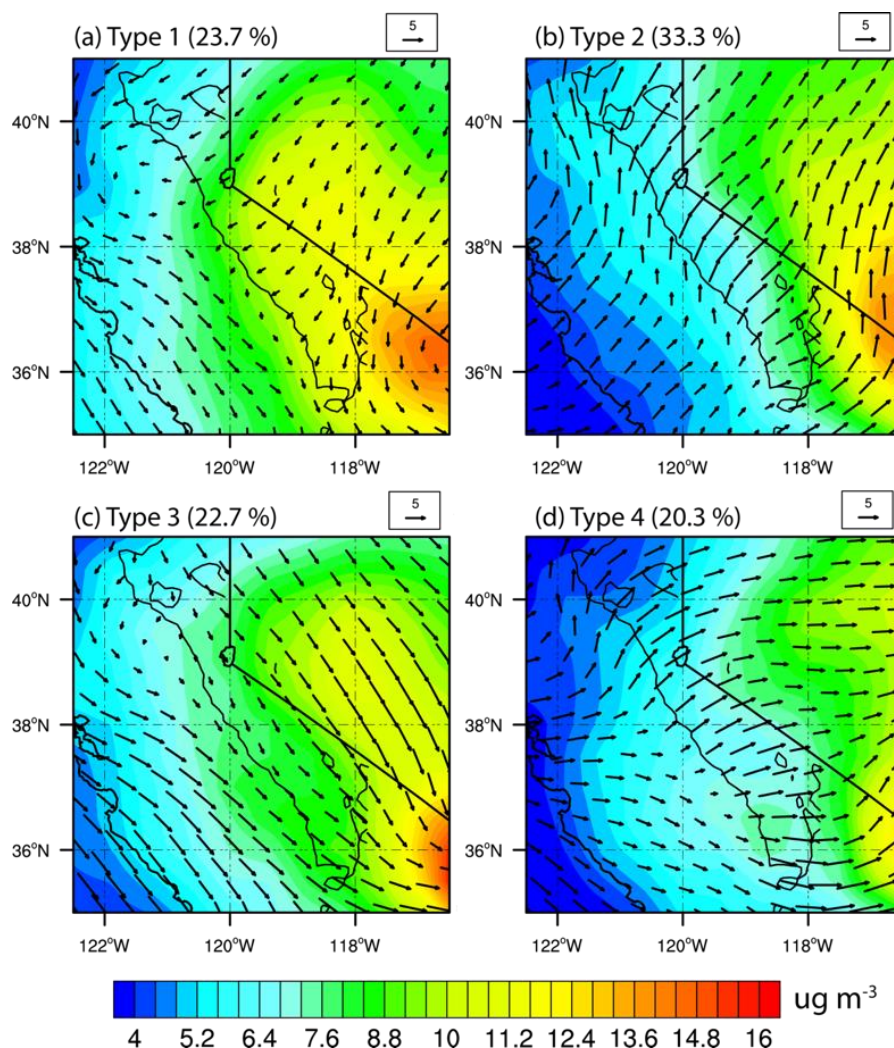
433 The averaged contribution of wet depositions in magnitude increases from 19% in all events to 29% in the
434 top 10 percentile, 36% in the top 5 percentile, and 56% in the top 1 percentile largest events, supporting
435 our conclusion that wet deposition is a more efficient way of dust deposition.



436
 437 **Figure 10** (a) Distribution of contribution of wet and dry depositions to total deposition in each type in
 438 WRF-Chem. (b) Distribution of contribution of wet and dry depositions to total deposition for all deposition,
 439 depositions over 90th, 95th, and 99th percentile. The three lines inside violin plot (a-b) indicate 25%, 50%,
 440 75% of the distribution
 441

442 3.4 Features of the dust transport in MERRA-2

443 We repeated the SOM analyses using 2019 MERRA-2 data to examine the WRF-Chem model
 444 performance and interannual variability. We conducted additional SOM analyses using 2011-2021
 445 climatology MERRA-2 data to investigate the interannual variability of the transport patterns. The low-
 446 level and mid-level dust transport features identified in MERRA-2 (Figs. 11-12) are similar to their
 447 corresponding types in WRF-Chem (Fig. 3), with types 1, 2, 3, and 4 representing MSR, SBJ-related, NPH-
 448 related and CPZ transport, respectively (Fig. 11). Additionally, north-south transport occurs in the middle
 449 layer in type 3 and west-east transport in type 4, despite the slight difference in the peak region (Fig. 12).

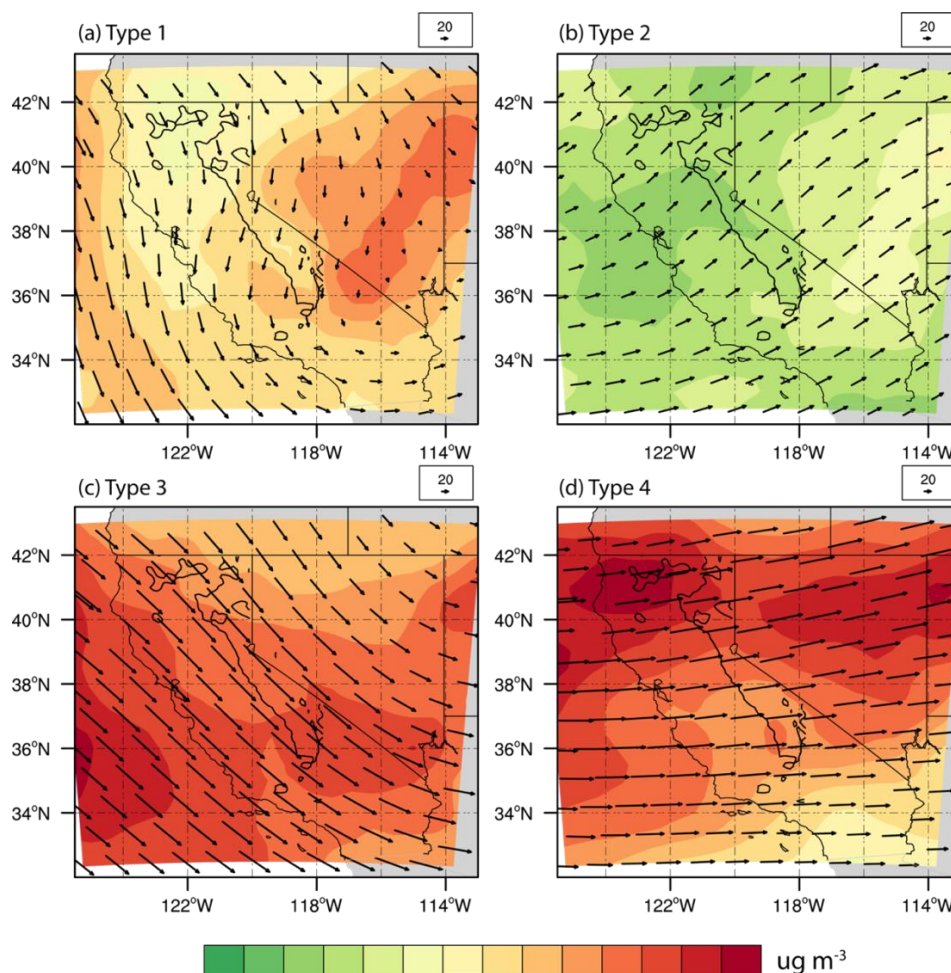


450

451

452

Figure 11 Low-level dust concentration ($\mu\text{g m}^{-3}$) and wind vectors (m s^{-1}) in each of the four SOM types from MERRA-2 for the year 2019. The numbers on the top of subplots denote the frequency of each type.



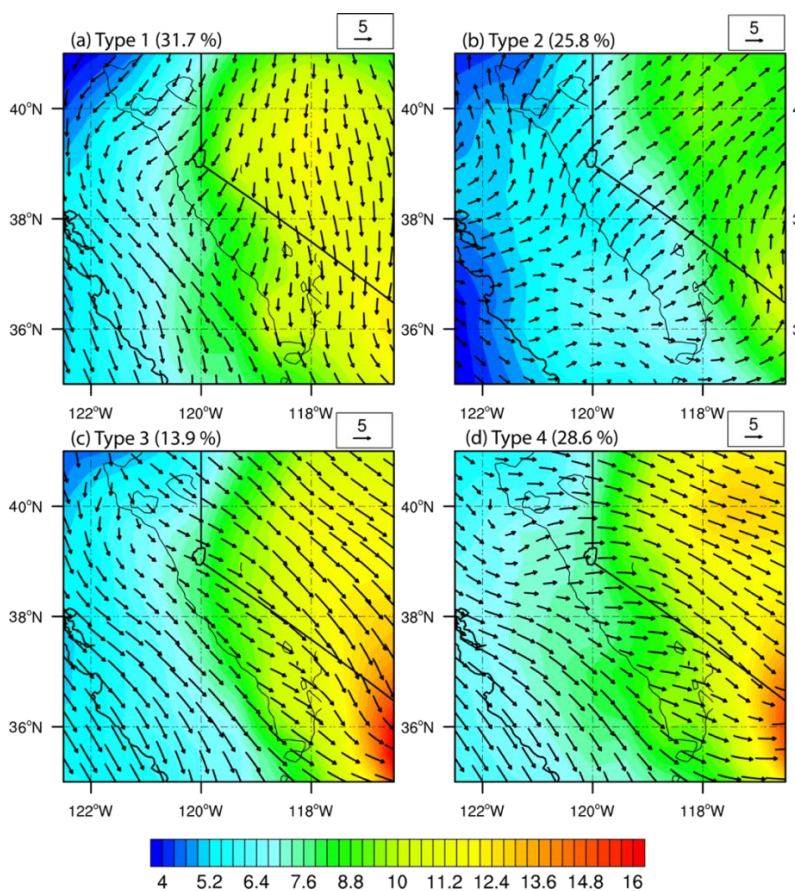
453
 454 **Figure 12** Mid-level (200-700 hPa average) dust concentration (ug m^{-3}) and dust transport fluxes (ug m^{-2})
 455 s^{-1}) in each of the four SOM types from MERRA-2 for the year 2019
 456

457 The relative contribution of each transport type in MERRA-2 (SBJ-related > MSR > CPZ > NPH-
 458 related) is generally consistent with the results in WRF-Chem (MSR > SBJ-related > CPZ > NPH-related),
 459 except that the MSR transport occurs less frequently in MERRA-2. The difference is largely caused by the
 460 spatial resolution of the two datasets. With a resolution of $0.5^\circ \times 0.625^\circ$, MERRA-2 has smooth topography
 461 information and cannot resolve the high peaks of the Sierra Nevada which produce the MSR winds and
 462 transport. Consequently, MSR transport contributes to a smaller fraction in the MERRA-2. The coarser



463 resolution MERRA-2 also produces a more homogeneous dust concentration at low levels than 2-km WRF-
 464 Chem.

465 Similar dust concentrations and transport patterns are found in the 11-year SOM analysis (Fig. 13),
 466 indicating that the four patterns identified in 2019 are representative of the climatological conditions. In
 467 climatology, the SBJ is weaker and air inflows hit the California coast at a further north latitude (about
 468 40 °N; Fig. 13b), which is reasonable as 2019 is a typical El Nino year with stronger AR reaching California
 469 further south than usual. The changes in the transport patterns reflect the interannual variations of large-
 470 scale forcings and regional weather conditions.



471 **Figure 13** Low level dust concentration ($\mu\text{g m}^{-3}$) and wind vectors (m s^{-1}) in each of the four SOM types
 472 from MERRA-2 averaged over 2011-2021. The numbers on the top right of subplots denote the frequency
 473 of each type.
 474
 475



476 **4. Conclusions and discussion**



477 **Figure 14** Schematic diagram of typical dust transport patterns across the Sierra Nevada. The “MSR”
478 demotes mesoscale regional transport. The “SBJ” and “NPH” denotes dust transport dominated by Sierra-
479 Block Jets (SBJ) and North Pacific High (NPH), respectively, while the “CPZ” denotes Cross-Pacific Zonal
480 transport.
481
482

483 With a focus on the dust that influences the mountain snow, we investigated the dust sources
484 surrounding the Sierra Nevada and their typical transport patterns during the spring and early summer.
485 Despite the strongest emissions from the Mojave Desert, dust is only transported northward to the mountain
486 when the mesoscale weather pattern dominates the southwest U.S. (Fig. 14). During 64.25% of our study
487 period, dust from the Mojave Desert is transported away from the mountains. Dust emitted from the Great
488 Basin is transported to the central Sierra Nevada during MSR transport and to the eastern part when the



489 NPH builds in the eastern Pacific. It is blown eastward by air inflows from the ocean during SBJ or cross-
490 Pacific transport. In contrast, dust produced by the Central Valley is persistently transported to the west
491 mountain slope, playing an essential role in snow impurities there. Carried by intense air inflows, it can be
492 transported to the eastern slope of the Sierra Nevada.

493 During April, Asia dust is transported zonally over the North Pacific through the straight zonal
494 isobars at the middle level. The dust layer descends to 800 hPa when it reaches the California coast. In the
495 presence of the NPH, dust emitted from Asia excurses north into Alaska/Canada and travels south along
496 the U.S. west coast. The dust travels at a higher altitude, and the concentrations are weaker than the zonal
497 transport.

498 Large amounts of depositions are found on the west slope, which generally decrease with elevations.
499 Dust particles transported to the higher altitude are small in size and difficult to deposit through gravitational
500 effects. The SBJ-produced AR collects dust in the rain and snow and deposits it on the high mountain.
501 Besides, considerable depositions occur when the elevated dust layer from the Pacific collides with the
502 mountain.

503 We acknowledge that our characterization of dominant transport patterns might be limited by model
504 uncertainties. Besides, the coarse-resolution reanalyses data, MERRA-2, cannot accurately resolve the
505 topography effects and tends to underestimate mesoscale regional transport. Furthermore, both WRF-Chem
506 and MERRA-2 describe dust emissions from dryland by relating them to high wind speed, soil moisture,
507 and soil type (Ginoux et al., 2001), while dust emission from agricultural lands is not specifically
508 implemented. However, a comprehensive evaluation of airborne dust and PM_{2.5} concentration between
509 model simulation and site observations in our previous study shows a good agreement between both (Huang
510 et al., 2022a). In addition, the dust transport pathways have well-defined patterns associated with the
511 mesoscale and large-scale weather systems. The general consistency across different models (WRF-Chem
512 and MERRA-2) and observations (satellite analysis) and across different years give us confidence that the
513 results are valid despite model uncertainties.



514 The analyses of dust emission and transport can be used to understand dust transport in a changing
515 climate. Studies have shown that global warming continues to dry the soil, producing more dust emissions
516 over the western U.S. Nevertheless, the change in transport and deposition patterns has not been well
517 recognized. Our study highlighted the connection between dust transport and dominant weather patterns
518 across the Sierra Nevada; the latter might respond in a more predictable way to climate change. Future
519 projections show that global warming may increase the frequency of landfalling AR by 20-35% by the end
520 of the 21st century (Hagos et al., 2016; Rhoades et al., 2021). Besides, the widening of the Hadley Cell in
521 response to global warming might enhance the NPH and shift it poleward (Song et al., 2018; Choi et al.,
522 2016). Thus said, the SBJ- and NPH-related dust transport may occur more frequently while the MSR
523 transport may become less common. In this regard, changes in dust emissions from the Central Valley might
524 play a more critical role in mountain snow impurities than those from the Mojave Desert and the Great
525 Basin, producing more depositions on the west slope of the Sierra Nevada.

526

527 **Data availability:**

528 The IASI DOD data is acquired from <https://iasi.aeris-data.fr/dust-aod/>. The MIDAS DOD is acquired from
529 <https://zenodo.org/record/4244106#.YsJqe-zMIws>. MERRA-2 aerosol reanalyses are available from
530 <https://disc.gsfc.nasa.gov/datasets?keywords=MERRA2&page=1> and ERA5 wind reanalyses are available
531 from <https://rda.ucar.edu/datasets/ds633.0/>. The WRF-Chem and MERRA-2 SOM clustering results have
532 been uploaded to <https://doi.org/10.5281/zenodo.6795994>.

533

534 **Author contributions:**

535 HH performed the analysis and drafted the manuscript. The methodology was developed by HH and YL.
536 JZ and AG provided the observational data used for model validation. YQ, CH, and ZZ helped with the
537 analysis and offered valuable comments. All authors contributed to writing and editing the manuscript.

538

539 **Competing interests:**



540 The authors declare that they have no conflict of interest.

541

542 **Acknowledgement:**

543 This research was supported by NASA awards: 80NSSC21K0997, 80NSSC20K1722, 80NSSC20K1349,

544 and 80NSSC18K1489. Antonis Gkikas was supported by the Hellenic Foundation for Research and

545 Innovation (H.F.R.I.) under the “2nd Call for H.F.R.I. Research Projects to support Post-Doctoral

546 Researchers” (project acronym: ATLANTAS, project number: 544). The Pacific Northwest National

547 Laboratory (PNNL) is operated for DOE by the Battelle Memorial Institute under contract DE-AC05-

548 76RLO1830.



549 Reference:

- 550 Aarons, S. M., Arvin, L. J., Aciego, S. M., Riebe, C. S., Johnson, K. R., Blakowski, M. A., Koornneef,
551 J. M., Hart, S. C., Barnes, M. E., Dove, N., Botthoff, J. K., Maltz, M., and Aronson, E. L.: Competing
552 droughts affect dust delivery to Sierra Nevada, *Aeolian Research*, 41, 100545,
553 <https://doi.org/10.1016/j.aeolia.2019.100545>, 2019.
- 554 Achakulwisut, P., Shen, L., and Mickley, L. J.: What Controls Springtime Fine Dust Variability in the
555 Western United States? Investigating the 2002–2015 Increase in Fine Dust in the U.S. Southwest,
556 *Journal of Geophysical Research: Atmospheres*, 122, 12,449–412,467,
557 <https://doi.org/10.1002/2017JD027208>, 2017.
- 558 Aciego, S. M., Riebe, C. S., Hart, S. C., Blakowski, M. A., Carey, C. J., Aarons, S. M., Dove, N. C.,
559 Botthoff, J. K., Sims, K. W. W., and Aronson, E. L.: Dust outpaces bedrock in nutrient supply to
560 montane forest ecosystems, *Nat Commun*, 8, 14800, [10.1038/ncomms14800](https://doi.org/10.1038/ncomms14800), 2017.
- 561 Ault, A. P., Williams, C. R., White, A. B., Neiman, P. J., Creamean, J. M., Gaston, C. J., Ralph, F. M.,
562 and Prather, K. A.: Detection of Asian dust in California orographic precipitation, *Journal of*
563 *Geophysical Research: Atmospheres*, 116, <https://doi.org/10.1029/2010JD015351>, 2011.
- 564 Bao, J.-W., Michelson, S. A., Persson, P. O. G., Djalalova, I. V., and Wilczak, J. M.: Observed and
565 WRF-Simulated Low-Level Winds in a High-Ozone Episode during the Central California Ozone
566 Study, *Journal of Applied Meteorology and Climatology*, 47, 2372–2394,
567 [10.1175/2008jamc1822.1](https://doi.org/10.1175/2008jamc1822.1), 2008.
- 568 Bao, M. and Wallace, J. M.: Cluster Analysis of Northern Hemisphere Wintertime 500-hPa Flow
569 Regimes during 1920–2014, *J Atmos Sci*, 72, 3597–3608, [10.1175/JAS-D-15-0001.1](https://doi.org/10.1175/JAS-D-15-0001.1), 2015.
- 570 Brahney, J., Ballantyne, A. P., Sievers, C., and Neff, J. C.: Increasing Ca²⁺ deposition in the western
571 US: The role of mineral aerosols, *Aeolian Research*, 10, 77–87,
572 <https://doi.org/10.1016/j.aeolia.2013.04.003>, 2013.
- 573 Buchard, V., da Silva, A. M., Randles, C. A., Colarco, P., Ferrare, R., Hair, J., Hostetler, C., Tackett,
574 J., and Winker, D.: Evaluation of the surface PM_{2.5} in Version 1 of the NASA MERRA Aerosol
575 Reanalysis over the United States, *Atmos Environ*, 125, 100–111,
576 <https://doi.org/10.1016/j.atmosenv.2015.11.004>, 2016.
- 577 Buchard, V., Randles, C. A., da Silva, A. M., Darmenov, A., Colarco, P. R., Govindaraju, R., Ferrare,
578 R., Hair, J., Beyersdorf, A. J., Ziemba, L. D., and Yu, H.: The MERRA-2 Aerosol Reanalysis, 1980
579 Onward. Part II: Evaluation and Case Studies, *J Climate*, 30, 6851–6872, [10.1175/JCLI-D-16-0613.1](https://doi.org/10.1175/JCLI-D-16-0613.1),
580 2017.
- 581 Buchholz, R., Emmons, L., and Tilmes, S.: CESM2. 1/CAM-chem instantaneous output for
582 boundary conditions, in: UCAR/NCAR-Atmospheric Chemistry Observations and Modeling
583 Laboratory, 2019.
- 584 Capelle, V., Chédin, A., Pondrom, M., Crevoisier, C., Armante, R., Crepeau, L., and Scott, N. A.:
585 Infrared dust aerosol optical depth retrieved daily from IASI and comparison with AERONET over
586 the period 2007–2016, *Remote Sens Environ*, 206, 15–32,
587 <https://doi.org/10.1016/j.rse.2017.12.008>, 2018.
- 588 Capelle, V., Chédin, A., Siméon, M., Tsamalis, C., Pierangelo, C., Pondrom, M., Crevoisier, C.,
589 Crepeau, L., and Scott, N. A.: Evaluation of IASI-derived dust aerosol characteristics over the
590 tropical belt, *Atmos. Chem. Phys.*, 14, 9343–9362, [10.5194/acp-14-9343-2014](https://doi.org/10.5194/acp-14-9343-2014), 2014.



- 591 Chapman, E. G., Gustafson, W. I., Easter, R. C., Barnard, J. C., Ghan, S. J., Pekour, M. S., and Fast,
592 J. D.: Coupling aerosol-cloud-radiative processes in the WRF-Chem model: Investigating the
593 radiative impact of elevated point sources, *Atmos Chem Phys*, 9, 945-964, 10.5194/acp-9-945-
594 2009, 2009.
- 595 Chin, M., Diehl, T., Ginoux, P., and Malm, W.: Intercontinental transport of pollution and dust
596 aerosols: implications for regional air quality, *Atmos. Chem. Phys.*, 7, 5501-5517, 10.5194/acp-7-
597 5501-2007, 2007.
- 598 Chin, M., Ginoux, P., Kinne, S., Torres, O., Holben, B. N., Duncan, B. N., Martin, R. V., Logan, J. A.,
599 Higurashi, A., and Nakajima, T.: Tropospheric Aerosol Optical Thickness from the GOCART Model
600 and Comparisons with Satellite and Sun Photometer Measurements, *J Atmos Sci*, 59, 461-483,
601 10.1175/1520-0469(2002)059<0461:Taotft>2.0.Co;2, 2002.
- 602 Choi, J., Lu, J., Son, S. W., Frierson, D. M., and Yoon, J. H.: Uncertainty in future projections of the
603 North Pacific subtropical high and its implication for California winter precipitation change,
604 *Journal of Geophysical Research: Atmospheres*, 121, 795-806, 2016.
- 605 Clausnitzer, H. and Singer, M. J.: Environmental influences on respirable dust production from
606 agricultural operations in California, *Atmos Environ*, 34, 1739-1745,
607 [https://doi.org/10.1016/S1352-2310\(99\)00385-4](https://doi.org/10.1016/S1352-2310(99)00385-4), 2000.
- 608 Creamean, J. M., Spackman, J. R., Davis, S. M., and White, A. B.: Climatology of long-range
609 transported Asian dust along the West Coast of the United States, *Journal of Geophysical*
610 *Research: Atmospheres*, 119, 12,171-112,185, <https://doi.org/10.1002/2014JD021694>, 2014.
- 611 Creamean, J. M., Suski, K. J., Rosenfeld, D., Cazorla, A., DeMott, P. J., Sullivan, R. C., White, A. B.,
612 Ralph, F. M., Minnis, P., and Comstock, J. M.: Dust and biological aerosols from the Sahara and
613 Asia influence precipitation in the western US, *Science*, 339, 1572-1578, 2013.
- 614 Crooks, J. L., Cascio, W. E., Percy, M. S., Reyes, J., Neas, L. M., and Hilborn, E. D.: The Association
615 between Dust Storms and Daily Non-Accidental Mortality in the United States,
616 1993–2005, *Environ Health Persp*, 124, 1735-1743, doi:10.1289/EHP216, 2016.
- 617 Duniway, M. C., Pfenninger, A. A., Fick, S. E., Nauman, T. W., Belnap, J., and Barger, N. N.: Wind
618 erosion and dust from US drylands: a review of causes, consequences, and solutions in a changing
619 world, *Ecosphere*, 10, e02650, <https://doi.org/10.1002/ecs2.2650>, 2019.
- 620 Easter, R. C., Ghan, S. J., Zhang, Y., Saylor, R. D., Chapman, E. G., Laulainen, N. S., Abdul-Razzak,
621 H., Leung, L. R., Bian, X. D., and Zaveri, R. A.: MIRAGE: Model description and evaluation of
622 aerosols and trace gases, *J Geophys Res-Atmos*, 109, ArtD20210
623 10.1029/2004jd004571, 2004.
- 624 Emmons, L. K., Schwantes, R. H., Orlando, J. J., Tyndall, G., Kinnison, D., Lamarque, J. F., Marsh,
625 D., Mills, M. J., Tilmes, S., Bardeen, C., Buchholz, R. R., Conley, A., Gettelman, A., Garcia, R.,
626 Simpson, I., Blake, D. R., Meinardi, S., and Petron, G.: The Chemistry Mechanism in the
627 Community Earth System Model Version 2 (CESM2), *J Adv Model Earth Sy*, 12, e2019MS001882,
628 ARTN e2019MS001882
629 10.1029/2019MS001882, 2020.
- 630 Forster, P., Ramaswamy, V., Artaxo, P., Berntsen, T., Betts, R., Fahey, D. W., Haywood, J., Lean, J.,
631 Lowe, D. C., and Myhre, G.: Changes in atmospheric constituents and in radiative forcing. Chapter
632 2, in: *Climate change 2007. The physical science basis*, 2007.
- 633 Gelaro, R., McCarty, W., Suárez, M. J., Todling, R., Molod, A., Takacs, L., Randles, C. A., Darmenov,
634 A., Bosilovich, M. G., Reichle, R., Wargan, K., Coy, L., Cullather, R., Draper, C., Akella, S., Buchard,



- 635 V., Conaty, A., da Silva, A. M., Gu, W., Kim, G.-K., Koster, R., Lucchesi, R., Merkova, D., Nielsen, J.
636 E., Partyka, G., Pawson, S., Putman, W., Rienecker, M., Schubert, S. D., Sienkiewicz, M., and Zhao,
637 B.: The Modern-Era Retrospective Analysis for Research and Applications, Version 2 (MERRA-2),
638 J Climate, 30, 5419-5454, 10.1175/jcli-d-16-0758.1, 2017.
- 639 Ginoux, P., Prospero, J. M., Gill, T. E., Hsu, N. C., and Zhao, M.: Global-scale attribution of
640 anthropogenic and natural dust sources and their emission rates based on MODIS Deep Blue
641 aerosol products, Reviews of Geophysics, 50, <https://doi.org/10.1029/2012RG000388>, 2012.
- 642 Ginoux, P., Chin, M., Tegen, I., Prospero, J. M., Holben, B., Dubovik, O., and Lin, S. J.: Sources and
643 distributions of dust aerosols simulated with the GOCART model, J Geophys Res-Atmos, 106,
644 20255-20273, Doi 10.1029/2000jd000053, 2001.
- 645 Gkikas, A., Proestakis, E., Amiridis, V., Kazadzis, S., Di Tomaso, E., Marinou, E., Hatzianastassiou,
646 N., Kok, J. F., and García-Pando, C. P.: Quantification of the dust optical depth across
647 spatiotemporal scales with the MIDAS global dataset (2003–2017), Atmos. Chem. Phys., 22, 3553-
648 3578, 10.5194/acp-22-3553-2022, 2022.
- 649 Gkikas, A., Proestakis, E., Amiridis, V., Kazadzis, S., Di Tomaso, E., Tsekeri, A., Marinou, E.,
650 Hatzianastassiou, N., and Pérez García-Pando, C.: Modls Dust AeroSol (MIDAS): a global fine-
651 resolution dust optical depth data set, Atmos. Meas. Tech., 14, 309-334, 10.5194/amt-14-309-
652 2021, 2021.
- 653 Goldstein, H. L., Breit, G. N., and Reynolds, R. L.: Controls on the chemical composition of saline
654 surface crusts and emitted dust from a wet playa in the Mojave Desert (USA), J Arid Environ, 140,
655 50-66, <https://doi.org/10.1016/j.jaridenv.2017.01.010>, 2017.
- 656 Hagos, S. M., Leung, L. R., Yoon, J.-H., Lu, J., and Gao, Y.: A projection of changes in landfalling
657 atmospheric river frequency and extreme precipitation over western North America from the
658 Large Ensemble CESM simulations, Geophys Res Lett, 43, 1357-1363,
659 <https://doi.org/10.1002/2015GL067392>, 2016.
- 660 Hand, J. L., Gill, T. E., and Schichtel, B. A.: Spatial and seasonal variability in fine mineral dust and
661 coarse aerosol mass at remote sites across the United States, Journal of Geophysical Research:
662 Atmospheres, 122, 3080-3097, <https://doi.org/10.1002/2016JD026290>, 2017.
- 663 Hand, J. L., White, W. H., Gebhart, K. A., Hyslop, N. P., Gill, T. E., and Schichtel, B. A.: Earlier onset
664 of the spring fine dust season in the southwestern United States, Geophys Res Lett, 43, 4001-
665 4009, <https://doi.org/10.1002/2016GL068519>, 2016.
- 666 Haywood, J. M., Allan, R. P., Culverwell, I., Slingo, T., Milton, S., Edwards, J., and Clerbaux, N.: Can
667 desert dust explain the outgoing longwave radiation anomaly over the Sahara during July 2003?,
668 Journal of Geophysical Research: Atmospheres, 110, <https://doi.org/10.1029/2004JD005232>,
669 2005.
- 670 Hersbach, H., Bell, B., Berrisford, P., Hirahara, S., Horanyi, A., Muñoz-Sabater, J., Nicolas, J.,
671 Peubey, C., Radu, R., Schepers, D., Simmons, A., Soci, C., Abdalla, S., Abellan, X., Balsamo, G.,
672 Bechtold, P., Biavati, G., Bidlot, J., Bonavita, M., De Chiara, G., Dahlgren, P., Dee, D., Diamantakis,
673 M., Dragani, R., Flemming, J., Forbes, R., Fuentes, M., Geer, A., Haimberger, L., Healy, S., Hogan,
674 R. J., Holm, E., Janiskova, M., Keeley, S., Laloyaux, P., Lopez, P., Lupu, C., Radnoti, G., de Rosnay,
675 P., Rozum, I., Vamborg, F., Villaume, S., and Thepaut, J. N.: The ERA5 global reanalysis, Q J Roy
676 Meteor Soc, 146, 1999-2049, 10.1002/qj.3803, 2020.
- 677 Hilton, F., Armante, R., August, T., Barnet, C., Bouchard, A., Camy-Peyret, C., Capelle, V., Clarisse,
678 L., Clerbaux, C., Coheur, P.-F., Collard, A., Crevoisier, C., Dufour, G., Edwards, D., Faijan, F., Fourrié,



- 679 N., Gambacorta, A., Goldberg, M., Guidard, V., Hurtmans, D., Illingworth, S., Jacquinet-Husson,
680 N., Kerzenmacher, T., Klaes, D., Lavanant, L., Masiello, G., Matricardi, M., McNally, A., Newman,
681 S., Pavelin, E., Payan, S., Péquignot, E., Peyridieu, S., Phulpin, T., Remedios, J., Schlüssel, P., Serio,
682 C., Strow, L., Stubenrauch, C., Taylor, J., Tobin, D., Wolf, W., and Zhou, D.: Hyperspectral Earth
683 Observation from IASI: Five Years of Accomplishments, *B Am Meteorol Soc*, 93, 347-370,
684 10.1175/BAMS-D-11-00027.1, 2012.
- 685 Huang, H., Gu, Y., Xue, Y., Jiang, J., and Zhao, B.: Assessing aerosol indirect effect on clouds and
686 regional climate of East/South Asia and West Africa using NCEP GFS, *Clim Dyn*, 52, 5759-5774,
687 10.1007/s00382-018-4476-9, 2019.
- 688 Huang, H., Qian, Y., He, C., Bair, E. H., and Rittger, K.: Snow Albedo Feedbacks Enhance Snow
689 Impurity-Induced Radiative Forcing in the Sierra Nevada, *Geophys Res Lett*, 49, e2022GL098102,
690 <https://doi.org/10.1029/2022GL098102>, 2022a.
- 691 Huang, H., Fischella, M. R., Liu, Y., Ban, Z., Fayne, J. V., Li, D., Cavanaugh, K. C., and Lettenmaier,
692 D. P.: Changes in Mechanisms and Characteristics of Western U.S. Floods Over the Last Sixty Years,
693 *Geophys Res Lett*, 49, e2021GL097022, 10.1029/2021gl097022, 2022b.
- 694 Hunt, W. H., Winker, D. M., Vaughan, M. A., Powell, K. A., Lucker, P. L., and Weimer, C.: CALIPSO
695 Lidar Description and Performance Assessment, *Journal of Atmospheric and Oceanic Technology*,
696 26, 1214-1228, 10.1175/2009jtecha1223.1, 2009.
- 697 Jardine, G. E., Crocker, A. J., Bailey, I., Cooper, M. J., Milton, J. A., and Wilson, P. A.: The imprint
698 of windblown dust from the North American Southwest on the California Channel Islands and
699 Pacific Ocean sediments, *Quaternary Science Reviews*, 261, 106934,
700 <https://doi.org/10.1016/j.quascirev.2021.106934>, 2021.
- 701 Kim, D., Chin, M., Cruz, C. A., Tong, D., and Yu, H.: Spring Dust in Western North America and Its
702 Interannual Variability—Understanding the Role of Local and Transported Dust, *Journal of*
703 *Geophysical Research: Atmospheres*, 126, e2021JD035383,
704 <https://doi.org/10.1029/2021JD035383>, 2021.
- 705 Kim, M. H., Omar, A. H., Tackett, J. L., Vaughan, M. A., Winker, D. M., Trepte, C. R., Hu, Y., Liu, Z.,
706 Poole, L. R., Pitts, M. C., Kar, J., and Magill, B. E.: The CALIPSO version 4 automated aerosol
707 classification and lidar ratio selection algorithm, *Atmos. Meas. Tech.*, 11, 6107-6135,
708 10.5194/amt-11-6107-2018, 2018.
- 709 Laden, F., Schwartz, J., Speizer, F. E., and Dockery, D. W.: Reduction in fine particulate air pollution
710 and mortality: Extended follow-up of the Harvard Six Cities study, *Am J Respir Crit Care Med*, 173,
711 667-672, 10.1164/rccm.200503-443OC, 2006.
- 712 Lei, H. and Wang, J. X. L.: Observed characteristics of dust storm events over the western United
713 States using meteorological, satellite, and air quality measurements, *Atmos. Chem. Phys.*, 14,
714 7847-7857, 10.5194/acp-14-7847-2014, 2014.
- 715 Lim, S. S., Vos, T., Flaxman, A. D., Danaei, G., Shibuya, K., Adair-Rohani, H., AlMazroa, M. A.,
716 Amann, M., Anderson, H. R., Andrews, K. G., Aryee, M., Atkinson, C., Bacchus, L. J., Bahalim, A.
717 N., Balakrishnan, K., Balmes, J., Barker-Collo, S., Baxter, A., Bell, M. L., Blore, J. D., Blyth, F., Bonner,
718 C., Borges, G., Bourne, R., Boussinesq, M., Brauer, M., Brooks, P., Bruce, N. G., Brunekreef, B.,
719 Bryan-Hancock, C., Bucello, C., Buchbinder, R., Bull, F., Burnett, R. T., Byers, T. E., Calabria, B.,
720 Carapetis, J., Carnahan, E., Chafe, Z., Charlson, F., Chen, H., Chen, J. S., Cheng, A. T.-A., Child, J. C.,
721 Cohen, A., Colson, K. E., Cowie, B. C., Darby, S., Darling, S., Davis, A., Degenhardt, L., Dentener, F.,
722 Des Jarlais, D. C., Devries, K., Dherani, M., Ding, E. L., Dorsey, E. R., Driscoll, T., Edmond, K., Ali, S.



723 E., Engell, R. E., Erwin, P. J., Fahimi, S., Falder, G., Farzadfar, F., Ferrari, A., Finucane, M. M.,
724 Flaxman, S., Fowkes, F. G. R., Freedman, G., Freeman, M. K., Gakidou, E., Ghosh, S., Giovannucci,
725 E., Gmel, G., Graham, K., Grainger, R., Grant, B., Gunnell, D., Gutierrez, H. R., Hall, W., Hoek, H.
726 W., Hogan, A., Hosgood, H. D., Hoy, D., Hu, H., Hubbell, B. J., Hutchings, S. J., Ibeanusi, S. E.,
727 Jacklyn, G. L., Jasrasaria, R., Jonas, J. B., Kan, H., Kanis, J. A., Kassebaum, N., Kawakami, N., Khang,
728 Y.-H., Khatibzadeh, S., Khoo, J.-P., Kok, C., Laden, F., Lalloo, R., Lan, Q., Lathlean, T., Leasher, J. L.,
729 Leigh, J., Li, Y., Lin, J. K., Lipshultz, S. E., London, S., Lozano, R., Lu, Y., Mak, J., Malekzadeh, R.,
730 Mallinger, L., Marcenes, W., March, L., Marks, R., Martin, R., McGale, P., McGrath, J., Mehta, S.,
731 Memish, Z. A., Mensah, G. A., Merriman, T. R., Micha, R., Michaud, C., Mishra, V., Hanafiah, K. M.,
732 Mokdad, A. A., Morawska, L., Mozaffarian, D., Murphy, T., Naghavi, M., Neal, B., Nelson, P. K.,
733 Nolla, J. M., Norman, R., Olives, C., Omer, S. B., Orchard, J., Osborne, R., Ostro, B., Page, A.,
734 Pandey, K. D., Parry, C. D. H., Passmore, E., Patra, J., Pearce, N., Pelizzari, P. M., Petzold, M.,
735 Phillips, M. R., Pope, D., Pope, C. A., Powles, J., Rao, M., Razavi, H., Rehfues, E. A., Rehm, J. T.,
736 Ritz, B., Rivara, F. P., Roberts, T., Robinson, C., Rodriguez-Portales, J. A., Romieu, I., Room, R.,
737 Rosenfeld, L. C., Roy, A., Rushton, L., Salomon, J. A., Sampson, U., Sanchez-Riera, L., Sanman, E.,
738 Sapkota, A., Seedat, S., Shi, P., Shield, K., Shivakoti, R., Singh, G. M., Sleet, D. A., Smith, E., Smith,
739 K. R., Stapelberg, N. J. C., Steenland, K., Stöckl, H., Stovner, L. J., Straif, K., Straney, L., Thurston,
740 G. D., Tran, J. H., Van Dingenen, R., van Donkelaar, A., Veerman, J. L., Vijayakumar, L., Weintraub,
741 R., Weissman, M. M., White, R. A., Whiteford, H., Wiersma, S. T., Wilkinson, J. D., Williams, H. C.,
742 Williams, W., Wilson, N., Woolf, A. D., Yip, P., Zielinski, J. M., Lopez, A. D., Murray, C. J. L., and
743 Ezzati, M.: A comparative risk assessment of burden of disease and injury attributable to 67 risk
744 factors and risk factor clusters in 21 regions, 1990–2010: a systematic analysis for the Global
745 Burden of Disease Study 2010, *The Lancet*, 380, 2224–2260, [https://doi.org/10.1016/S0140-](https://doi.org/10.1016/S0140-6736(12)61766-8)
746 [6736\(12\)61766-8](https://doi.org/10.1016/S0140-6736(12)61766-8), 2012.

747 Liu, Y., Qian, Y., and Berg, L. K.: Local-thermal-gradient and large-scale-circulation impacts on
748 turbine-height wind speed forecasting over the Columbia River Basin, *Wind Energ. Sci.*, 7, 37–51,
749 10.5194/wes-7-37-2022, 2022.

750 Muhs, D. R., Budahn, J., Reheis, M., Beann, J., Skipp, G., and Fisher, E.: Airborne dust transport to
751 the eastern Pacific Ocean off southern California: Evidence from San Clemente Island, *Journal of*
752 *Geophysical Research: Atmospheres*, 112, <https://doi.org/10.1029/2006JD007577>, 2007.

753 Neff, J. C., Ballantyne, A. P., Farmer, G. L., Mahowald, N. M., Conroy, J. L., Landry, C. C., Overpeck,
754 J. T., Painter, T. H., Lawrence, C. R., and Reynolds, R. L.: Increasing eolian dust deposition in the
755 western United States linked to human activity, *Nat Geosci*, 1, 189–195, 10.1038/ngeo133, 2008.

756 Neiman, P. J., Hughes, M., Moore, B. J., Ralph, F. M., and Sukovich, E. M.: Sierra Barrier Jets,
757 Atmospheric Rivers, and Precipitation Characteristics in Northern California: A Composite
758 Perspective Based on a Network of Wind Profilers, *Mon Weather Rev*, 141, 4211–4233,
759 10.1175/mwr-d-13-00112.1, 2013.

760 Okin, G., Gillette, D., and Herrick, J.: Multi-scale controls on and consequences of aeolian
761 processes in landscape change in arid and semi-arid environments, *J Arid Environ*, 65, 253–275,
762 2006.

763 Pappagianis, D. and Einstein, H.: Tempest from Tehachapi takes toll or Coccidioides conveyed
764 aloft and afar, *Western Journal of Medicine*, 129, 527, 1978.

765 Pu, B. and Ginoux, P.: How reliable are CMIP5 models in simulating dust optical depth?, *Atmos.*
766 *Chem. Phys.*, 18, 12491–12510, 10.5194/acp-18-12491-2018, 2018.



- 767 Qian, Y., Gustafson, W. I., Leung, L. R., and Ghan, S. J.: Effects of soot-induced snow albedo change
768 on snowpack and hydrological cycle in western United States based on Weather Research and
769 Forecasting chemistry and regional climate simulations, *J Geophys Res-Atmos*, 114, Artn D03108
770 10.1029/2008jd011039, 2009.
- 771 Qian, Y., Yasunari, T. J., Doherty, S. J., Flanner, M. G., Lau, W. K. M., Ming, J., Wang, H., Wang, M.,
772 Warren, S. G., and Zhang, R.: Light-absorbing particles in snow and ice: Measurement and
773 modeling of climatic and hydrological impact, *Adv Atmos Sci*, 32, 64-91, 10.1007/s00376-014-
774 0010-0, 2014.
- 775 Randles, C. A., da Silva, A. M., Buchard, V., Colarco, P. R., Darmenov, A., Govindaraju, R., Smirnov,
776 A., Holben, B., Ferrare, R., Hair, J., Shinozuka, Y., and Flynn, C. J.: The MERRA-2 Aerosol Reanalysis,
777 1980 Onward. Part I: System Description and Data Assimilation Evaluation, *J Climate*, 30, 6823-
778 6850, 10.1175/JCLI-D-16-0609.1, 2017.
- 779 Reheis, M. C. and Kihl, R.: Dust Deposition in Southern Nevada and California, 1984-1989 -
780 Relations to Climate, Source Area, and Source Lithology, *J Geophys Res-Atmos*, 100, 8893-8918,
781 Doi 10.1029/94jd03245, 1995.
- 782 Reusch, D. B., Alley, R. B., and Hewitson, B. C.: North Atlantic climate variability from a self-
783 organizing map perspective, *Journal of Geophysical Research: Atmospheres*, 112,
784 <https://doi.org/10.1029/2006JD007460>, 2007.
- 785 Rhoades, A. M., Risser, M. D., Stone, D. A., Wehner, M. F., and Jones, A. D.: Implications of
786 warming on western United States landfalling atmospheric rivers and their flood damages,
787 *Weather Clim Extreme*, 32, 100326, <https://doi.org/10.1016/j.wace.2021.100326>, 2021.
- 788 Rodionov, S. N., Bond, N. A., and Overland, J. E.: The Aleutian Low, storm tracks, and winter
789 climate variability in the Bering Sea, *Deep Sea Research Part II: Topical Studies in Oceanography*,
790 54, 2560-2577, <https://doi.org/10.1016/j.dsr2.2007.08.002>, 2007.
- 791 Sarangi, C., Qian, Y., Rittger, K., Leung, L. R., Chand, D., Bormann, K. J., and Painter, T. H.: Dust
792 dominates high-altitude snow darkening and melt over high-mountain Asia, *Nat Clim Change*, 10,
793 1045-+, 10.1038/s41558-020-00909-3, 2020.
- 794 Skiles, S. M., Flanner, M., Cook, J. M., Dumont, M., and Painter, T. H.: Radiative forcing by light-
795 absorbing particles in snow, *Nat Clim Change*, 8, 964-971, 10.1038/s41558-018-0296-5, 2018.
- 796 Song, F., Leung, L. R., Lu, J., and Dong, L.: Future Changes in Seasonality of the North Pacific and
797 North Atlantic Subtropical Highs, *Geophys Res Lett*, 45, 11,959-911,968,
798 <https://doi.org/10.1029/2018GL079940>, 2018.
- 799 Song, F., Feng, Z., Leung, L. R., Houze Jr, R. A., Wang, J., Hardin, J., and Homeyer, C. R.: Contrasting
800 Spring and Summer Large-Scale Environments Associated with Mesoscale Convective Systems
801 over the U.S. Great Plains, *J Climate*, 32, 6749-6767, 10.1175/JCLI-D-18-0839.1, 2019.
- 802 Song, Q., Zhang, Z., Yu, H., Ginoux, P., and Shen, J.: Global dust optical depth climatology derived
803 from CALIOP and MODIS aerosol retrievals on decadal timescales: regional and interannual
804 variability, *Atmos. Chem. Phys.*, 21, 13369-13395, 10.5194/acp-21-13369-2021, 2021.
- 805 Tong, D. Q., Wang, J. X. L., Gill, T. E., Lei, H., and Wang, B.: Intensified dust storm activity and
806 Valley fever infection in the southwestern United States, *Geophys Res Lett*, 44, 4304-4312,
807 <https://doi.org/10.1002/2017GL073524>, 2017.
- 808 Vicars, W. C. and Sickman, J. O.: Mineral dust transport to the Sierra Nevada, California: Loading
809 rates and potential source areas, *J Geophys Res-Bioge*, 116, Artn G01018
810 10.1029/2010jg001394, 2011.



811 von Storch, H., Langenberg, H., and Feser, F.: A spectral nudging technique for dynamical
812 downscaling purposes, *Mon Weather Rev*, 128, 3664-3673, 2000.

813 Voss, K. K. and Evan, A. T.: A New Satellite-Based Global Climatology of Dust Aerosol Optical
814 Depth, *Journal of Applied Meteorology and Climatology*, 59, 83-102, 10.1175/JAMC-D-19-0194.1,
815 2020.

816 Voss, K. K., Evan, A. T., and Ralph, F. M.: Evaluating the Meteorological Conditions Associated
817 With Dusty Atmospheric Rivers, *Journal of Geophysical Research: Atmospheres*, 126,
818 e2021JD035403, <https://doi.org/10.1029/2021JD035403>, 2021.

819 Winker, D. M., Vaughan, M. A., Omar, A., Hu, Y., Powell, K. A., Liu, Z., Hunt, W. H., and Young, S.
820 A.: Overview of the CALIPSO Mission and CALIOP Data Processing Algorithms, *Journal of*
821 *Atmospheric and Oceanic Technology*, 26, 2310-2323, 10.1175/2009jtecha1281.1, 2009.

822 Winker, D. M., Pelon, J., Coakley, J. A., Ackerman, S. A., Charlson, R. J., Colarco, P. R., Flamant, P.,
823 Fu, Q., Hoff, R. M., Kittaka, C., Kubar, T. L., Le Treut, H., McCormick, M. P., Mégie, G., Poole, L.,
824 Powell, K., Trepte, C., Vaughan, M. A., and Wielicki, B. A.: The CALIPSO Mission: A Global 3D View
825 of Aerosols and Clouds, *B Am Meteorol Soc*, 91, 1211-1230, 10.1175/2010bams3009.1, 2010.

826 Wu, L., Su, H., Kalashnikova, O., Jiang, J., Zhao, C., Garay, M., Campbell, J., and Yu, N.: WRF-Chem
827 simulation of aerosol seasonal variability in the San Joaquin Valley, *Atmos Chem Phys*, 17, 7291-
828 7309, 10.5194/acp-17-7291-2017, 2017.

829 Wu, L., Gu, Y., Jiang, J., Su, H., Yu, N., Zhao, C., Qian, Y., Zhao, B., Liou, K., and Choi, Y.: Impacts of
830 aerosols on seasonal precipitation and snowpack in California based on convection-permitting
831 WRF-Chem simulations, *Atmos Chem Phys*, 18, 5529-5547, 10.5194/acp-18-5529-2018, 2018.

832 Young, S. A., Vaughan, M. A., Garnier, A., Tackett, J. L., Lambeth, J. D., and Powell, K. A.: Extinction
833 and optical depth retrievals for CALIPSO's Version 4 data release, *Atmos. Meas. Tech.*, 11, 5701-
834 5727, 10.5194/amt-11-5701-2018, 2018.

835 Yu, H., Tan, Q., Chin, M., Remer, L. A., Kahn, R. A., Bian, H., Kim, D., Zhang, Z., Yuan, T., Omar, A.
836 H., Winker, D. M., Levy, R. C., Kalashnikova, O., Crepeau, L., Capelle, V., and Chédin, A.: Estimates
837 of African Dust Deposition Along the Trans-Atlantic Transit Using the Decadelong Record of
838 Aerosol Measurements from CALIOP, MODIS, MISR, and IASI, *Journal of Geophysical Research:*
839 *Atmospheres*, 124, 7975-7996, <https://doi.org/10.1029/2019JD030574>, 2019.

840 Zaveri, R. A. and Peters, L. K.: A new lumped structure photochemical mechanism for large-scale
841 applications, *Journal of Geophysical Research: Atmospheres*, 104, 30387-30415, 1999.

842 Zheng, J., Zhang, Z., Garnier, A., Yu, H., Song, Q., Wang, C., Dubuisson, P., and Di Biagio, C.: The
843 thermal infrared optical depth of mineral dust retrieved from integrated CALIOP and IIR
844 observations, *Remote Sens Environ*, 270, 112841, <https://doi.org/10.1016/j.rse.2021.112841>,
845 2022.

846